Physics of Fluids

Drop impact onto polarized dielectric surface for controlled coating

Cite as: Phys. Fluids **33**, 062101 (2021); https://doi.org/10.1063/5.0054077
Submitted: 14 April 2021 . Accepted: 03 May 2021 . Published Online: 01 June 2021

A. Sankaran, J. Wu (经纬, 吴), R. Granda, V. Yurkiv, F. Mashayek, and A. L. Yarin

Physics of Fluids ARTICLE scitation.org/journal/phf

Drop impact onto polarized dielectric surface for controlled coating

Cite as: Phys. Fluids 33, 062101 (2021); doi: 10.1063/5.0054077
Submitted: 14 April 2021 · Accepted: 3 May 2021 ·
Published Online: 1 June 2021

A. Sankaran, J. Wu (经纬, 吴), R. Granda, V. Yurkiv, F. Mashayek, and A. L. Yarin[a)]

AFFILIATIONS

Department of Mechanical and Industrial Engineering, University of Illinois at Chicago, 842 W. Taylor St., Chicago, Illinois 60607-7022, USA

[a)]Author to whom correspondence should be addressed: ayarin@uic.edu

ABSTRACT

Control of surface wettability by means of electrowetting-on-dielectric (EWOD) is among the most effective methods of active enhancement of surface wettability. Here, electrohydrodynamics of drop impact onto a dielectric surface with electrodes embedded in the dielectric (or aligned and attached to it) is experimentally investigated. Drop impact of different liquids (water, n-butanol, and motor oil) onto different substrates (stretched Teflon, parafilm, and polypropylene) is studied. Water drop impact onto stretched Teflon (the only Teflon which revealed significant electrowetting) and un-stretched parafilm surfaces is studied in detail. The results for water drop impact indicate that drop spreading on such non-wettable surfaces can be significantly enhanced by the electric field application. In particular, water drop rebound can be suppressed by the electric force. Furthermore, impact dynamics and spreading of hydrocarbon liquids with electric field are explored. Partial suppression of splash phenomena was also observed with the application of the electric field in addition to enhancement of spreading. In addition, the experimental results for water drops are compared with the Cahn–Hilliard–Navier–Stokes (CHNS) simulations for static contact angles and drop impact dynamics, and the results are in close agreement for water drops. This study demonstrates that electrowetting-on-dielectric holds great promise for coating and spraying technologies.

I. INTRODUCTION

Controlled drop deposition onto a dry surface is important for technologies such as spray cooling, pesticide deposition, inkjet printing, spray painting, and coating.[1–6] Drop impact onto dry surfaces has received considerable attention of the research community and revealed a number of distinct flow patterns, such as prompt and corona splashing, receding breakup, partial rebound, and complete rebound in addition to deposition.[1,7] In general, the flow pattern depends on liquid properties, surface wettability, and the drop impact velocity. "Slippery surfaces" or surfaces that promote complete rebound of water have received significant attention for self-cleaning and anti-icing applications.[8–11] However, in coating and painting applications drop rebound and splashing limit the effectiveness as they increase the spraying costs due to material loss. The tendency to drop rebound was found to increase with the impact velocity, liquid surface tension, and the receding angle of the drop.[3,7]

Some of the ways to improve drop deposition onto surfaces explored in literature involve additives to liquid and surface modification.[12–16] Polymer additives change the rheological properties of the liquid, which has shown to prevent drop rebound from the surfaces.[12,13] In particular, the decrease in the drop retraction speed is attributed to the increase in elongational viscosity of dilute polymer solutions, which inhibits drop rebound.[13] The addition of surfactants leads to an improved wettability which hinders the rebound after impact.[14,15] A stretchable polymer substrate has also been shown to suppress drop rebound. This is attributed to transfer of a part of the drop kinetic energy to the deformation of the polymer surface affecting significantly the recoil behavior.[16] Furthermore, impact of ellipsoidal drops has been demonstrated to prevent drop rebound due to the axis switching during retraction.[17] This is accompanied by the kinetic energy being utilized for switching the deformation axes of the drop instead of rebound.[17]

Surface wettability is of significant importance in practical applications of spray coating, spray painting, adhesion, micro-fluidics, etc.[1–5] and is one of the fundamental aspects of dynamic behavior of drops during an impact onto dry solid surfaces. Wettability and surface adhesion are controlled by the surface chemistry and roughness. Control of surface wettability by means of electrowetting (EW) or electrowetting-on-dielectric (EWOD) is an attractive approach, which does not involve use of additional chemical agents.[18,19] Additionally,

in this case drop impact is controlled by the applied electric field and hence does not rely on the substrate modification. The EW or EWOD methods enhance liquid wettability on partially wettable or completely non-wettable surfaces. The EW is known to affect the equilibrium contact angle of drops.[18,19] The EW is associated with reduction in the solid–liquid interfacial energy due to the free ions reorganizing at the dielectric surface when voltage is applied to the surface. The EW is widely used to manipulate drops on surfaces, with the applications ranging from the "Lab-on-a-chip" microfluidics to optical applications.[20] However, drop impact is a dynamic situation which can be significantly disrupted by transient effects.

For coating applications, one is interested in controlled drop deposition with enhanced spreading and efficiency. One important question is whether one can reduce or completely prevent drop splashing and rebound associated with high impact velocities. The electric field-assisted manipulation of the impacting drops on the surface is an attractive approach aiming at an increase in the coating effectiveness. Several preliminary studies reveal a promising trend.[21,22] However, this effect certainly requires a further exploration of such aspects as an increase in the coating effectiveness with the application of the electric field. Drop impact onto stretched and un-stretched Teflon was investigated in Ref. 21. The rebound was suppressed by the application of the electric field.[21] The corresponding continuum modeling which reproduced similar trends is available.[22] Drop impact onto a concentric system of electrodes was numerically investigated in Ref. 23. The simulation results mimicked superhydrophobic behavior with the voltage application.

Additionally, there is an open question whether the dynamic electrowetting can prevent splashing during drop impact at a relatively high impact velocity. Splashing during drop impact onto a solid surface happens above the threshold based on the capillary number[24] $Ca^{1/2} = 0.35$. Here, the capillary number, $Ca = \mu V_0/\gamma$, where V_0 is the impact velocity, μ and γ are the liquid viscosity and surface tension, respectively. For water, this splashing threshold translates into a high impact velocity ~10 m/s. Another threshold for splash was proposed in Refs. 1, 2, 7, and 25. This threshold depends on the dimensionless number $K = WeOh^{-2/5}$, where Oh is the Ohnesorge number defined as $Oh = \mu/\sqrt{\rho D\gamma}$ and $We = \rho D V_0^2/\gamma$ is the Weber number, with ρ being liquid density, and D being the drop diameter. Using the K number, splashing phenomena observed on solid surfaces have been broadly classified as prompt splash and corona splash.[1,2,7,25] Prompt splash is characterized by secondary drops issued in the azimuthal directions from a spreading lamella emerging early after drop impact, whereas the corona splash is characterized by formation of a visible crown at an angle to the substrate relatively late after the impact.[1,2,7,25] Conclusive observations of prompt and corona splashes could require visualization from more than one direction.[25] Some efforts to delineate the regimes have been undertaken in Ref. 25.

Then, splash formation can be significant for low-surface tension liquids, for example, hydrocarbon liquids. Several different types of paints are utilized for spray painting, specifically, oil-based and water-based paints.[26,27] A variety of emulsions are used with different water-organic solvent ratios to optimize different characteristics of painting including cost, drying features, environmental aspects, etc.[27] Accordingly, it is tempting to explore the effect of the applied electric field in painting and coating applications.

Understanding the mechanism and control of splashing is desirable for the applications of spray coating and painting.[25,28] Furthermore, it is also important for understanding plant pathogen transport resulting from drop impact onto surfaces of leaves.[29,30] However, there are only scarce works related to suppressing of splashing. It has been found that drop splashing can be suppressed by reducing the surrounding gas pressure.[31] A hybrid surface designed with superhydrophobic/-philic pattern has been shown to suppress water drop splashing.[28] Still, splashing has been observed on both superhydrophobic and superhydrophilic surfaces. Furthermore, the impact dynamics also depends on the shape and size of the surface patterns.[28] Softer substrates have been reported to suppress splashing.[32] Other efforts related to splashing suppression involve addition of polymers or surfactants to the liquid.[33,34]

The present work explores the effect of the electric field on water drop impact dynamics in the case of dielectric non-wettable surfaces. The experiments are conducted using Teflon, parafilm and polypropylene surfaces with water being used as the working liquid. The experimental results for water drops are complemented by Cahn–Hilliard–Navier–Stokes (CHNS) numerical simulations following the method detailed in Ref. 22. Furthermore, the effect of the electric field on impact of n-butanol and motor oil drops is investigated.

II. METHODS

A. Experimental

The experimental setup is sketched in Fig. 1. The dielectric substrate (Teflon, parafilm, or polypropylene) was placed above two plane electrodes. The active surface for the drop impact was the area between the electrodes, whereas the rest of the surface was insulated by Kapton tape. The electrodes comprised two copper strips attached on a microscope glass slide at a pre-determined distance in-between. One of the electrodes was connected to a positive high voltage supply (custom built with a 0–20 kV range). The other copper electrode was grounded. The inter-electrode distance was 1.5 cm or 1.9 cm. The setup was enclosed on all sides (except the visualization windows) with metal sheet, which was grounded, thus forming a Faraday cage.

The glass slide with the substrate was mounted on an adjustable platform, which could be controlled in three axes using micrometers [Fig. 1(c)]. The stage control enabled positioning of the substrate along all the three directions. Additionally, a fine-tune control along the X-axis (one of the horizontal axes) allowed one to aim the center of the drop impact at the inter-electrode center. With different trials, it was noted that the deviation of the center of the impacting drop from the inter-electrode center was within 0.2 mm.

A laboratory syringe supplied water (or another working liquid) to the needle using syringe pump with a 90°-bent 27 gage needle. The out-of-focus 90°-bent 27 gage needle helped placing the camera right above to visualize the top view. The average diameters were about 2.5 mm, 1.87 mm, and 2.4 mm for water, n-butanol, and motor oil drops, respectively. The corresponding volumes are 8.2×10^{-3}, 3.4×10^{-3}, and 7.2×10^{-3} cm^3, respectively. The drops were gravity-driven and hence, the impact velocity was controlled by the height of the needle. Only normal drop impact is considered here.

The material properties of the working liquids used in experiments are listed in Table I.

Two high-speed cameras (Phantom v210 and Phantom Miro 4) were set up to visualize the side and top views of drop impact. For the

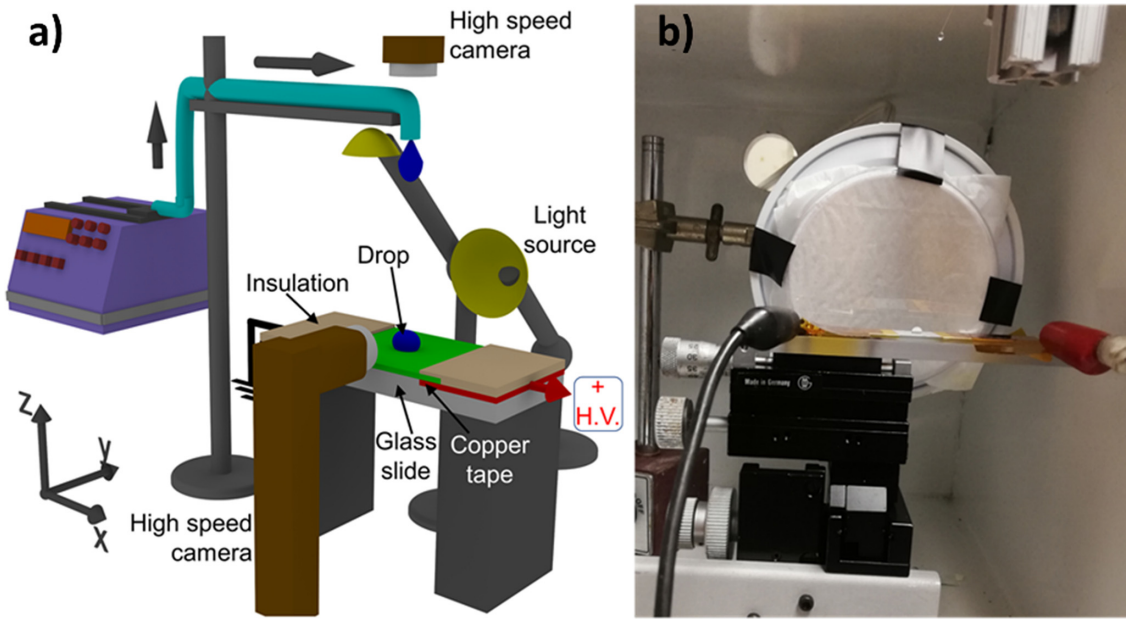

FIG. 1. (a) Schematic of the experimental setup; (b) photograph of the experimental setup from the direction of the high-speed camera.

side view, back lighting illuminated the drop, while for the top view front/back lighting was utilized [cf. Figs. 1(a) and 1(b)]. For contact angle measurements, the drop was softly deposited onto the surface. The images were analyzed in ImageJ, MATLAB and Adobe Photoshop. The velocity of impact was determined by the drop motion observed in the side view.

Teflon (PTFE) membrane (#6802K16) and polypropylene membrane (#7524T11) were obtained from Mcmaster Carr with the thickness of 0.081 mm and 0.051 mm, respectively. Parafilm M Laboratory Film was obtained from Bemis manufacturer (#PM992). It is referred to as parafilm here. The thickness of parafilm was 0.127 mm. Teflon membranes were pre-stretched by Instron machine (model 5942); the details are provided in Supplementary Information (SI); cf. Fig. S1. Furthermore, the SEM images of Teflon samples and parafilm are also provided in SI (cf. Figs. S2 and S3).

B. Modeling

The computational domain includes the full 3D-resolved single water drop on Teflon or parafilm surface (cf. Fig. S6 in SI). The medium consists of two phases: the first phase is the drop (liquid), and the second phase is the surrounding gas–phase (air). The phase-field model (PFM) is used to track the phases and the interfaces, and the Navier–Stokes (NS) equations are solved to model the two-phase flow of the liquid and gas phases. The free energy functional in the PFM is comprised of several contributions and described by the following equation:[35,36]

$$F(\bar{c},\varphi)=\int_V\left[f_{ch}(\bar{c})+\frac{1}{2}\varepsilon_{\bar{c}}\gamma_{\bar{c}}\alpha(\nabla\bar{c})^2+f_{elst}(\rho_V,\varphi)\right]\mathrm{d}V, \quad (1)$$

where V is the volume, $f_{ch}(\bar{c})$ is the chemical free energy density, with the variable $\bar{c}$ being used to model the two phases with two minima at $\bar{c}=-1$ (liquid) and $\bar{c}=1$ (the gas phase). The second term on the right–hand side in Eq. (1) accounts for the excess free energy due to the inhomogeneous distribution of $\bar{c}$ variable in the interfacial region. In addition, $\varepsilon_{\bar{c}}$ is the measure of the interface thickness, and $\gamma_{\bar{c}}$ is the effective surface tension coefficient. The constant α takes a value of $6\sqrt{2}$ following the work of Ding *et al.*[37] This term originates from the integration of the excess free energy per unit surface area across the drop interface. The function $f_{elst}(\rho_V,\varphi)$ describes the electrostatic energy density, which is calculated as follows:

$$f_{elst}(\rho_V,\varphi)=\frac{1}{2}\rho_V\varphi, \quad (2)$$

where ρ_V is the volumetric charge density, and φ is the potential.

TABLE I. Properties of liquids used in experiments.

Fluid/property	Density (kg/m^3)	Viscosity (Pa s)	Surface tension (mN/m)	Dielectric constant	Electrical conductivity (S/cm)
water	1000	8.9×10^{-4}	72	80	10^{-4}
n-butanol	810	2.6×10^{-3}	25	18	2×10^{-6}
motor oil	870	5.0×10^{-2}	30	2.3	2×10^{-10}

The NS equations are used to simulate the fluid flow and are coupled with the advective Cahn-Hilliard (CH) equation. The NS equations comprised of the mass balance (the continuity equation) and the momentum balance read

$$\nabla \cdot \mathbf{u} = 0, \tag{3}$$

$$\rho_F \left[\frac{\partial \mathbf{u}}{\partial t} + (\mathbf{u} \cdot \nabla)\mathbf{u}\right] = -\nabla p + \nabla \cdot \left[\mu(\nabla \mathbf{u} + \nabla \mathbf{u}^T)\right] + \boldsymbol{F}_{st} + \boldsymbol{F}_{elef} + \rho_F \boldsymbol{g}, \tag{4}$$

where $\mathbf{u}$ is the velocity vector, p is the pressure, ρ_F is the density of fluid, μ is the viscosity, $\boldsymbol{g}$ is the gravity acceleration, $\boldsymbol{F}_{st}$ is the surface tension force, and $\boldsymbol{F}_{elef}$ is the electrostatic force. A detailed description of the CH and NS equations' coupling, as well as their exchange terms and boundary conditions are given in our prior published work;[22] cf. Fig. S9 in SI for a brief overview.

III. RESULTS AND DISCUSSION

A. Static contact angle measurements

The static contact angle measurements were conducted on substrates with drops softly placed on them. The measurements were carried out using ImageJ tool. The reported contact angle is the average measured on both sides of the drop, with an error within $\pm 2^\circ$. The effect of gravity in these measurements is negligibly small because the Bond number[1] $Bo = \rho_F g D^2/\gamma \ll 1$, where D is the drop diameter and γ is the surface tension of liquid.

In order to validate the CHNS model and to better understand the influence of the applied voltage on drop shape, the CHNS calculations of the static contact angle are performed for 0 V, 8.5 kV and 9 kV voltage applied to the bottom of the dielectric substrate on one side and the ground attached on the opposite side (cf. Fig. 1). The initial conditions for all cases were identical: a cube with its height equal to the drop diameter of 2.5 mm. The initial velocities in both phases were set to zero (relaxation under the influence of gravity). From the physical point of view, the contact angle is considered as a measure of the homogeneous surface wettability. As usual, for the contact angle less than 90° the surface is considered to be partially wettable, i.e., hydrophilic. In contrast, for the angle larger than 90° the surface is non-wettable, i.e., hydrophobic.

The static contact angle with no applied voltage was found to decrease from the 25%-stretched Teflon to the 50%-stretched Teflon. In Ref. 21, it was found that the static contact angle of water on Teflon increased until the 200% stretching and then decreased. However, it should be emphasized that the contact angle variation is dependent on the microstructure and the corresponding roughness change. In the present work, with the application of voltage, it was found that the change of the water contact angle on Teflon was abrupt at the voltage of ~8.5–8.7 kV as the voltage was increased, as seen in the images in Figs. 2(a) and 3(a). In particular, for the 25%-stretched Teflon specimen presented in Fig. 2(a), the change occurred at ~8.7 kV, whereas for the 50%-stretched Teflon specimen the change occurred at ~8.5 kV. In the repeated experiments, the contact angle change occurred at similar applied voltages, albeit not necessarily at exactly the same values. In some cases, the contact angle of the water drop changed on the scale of seconds or faster at a fixed applied voltage. Overall, the experiments revealed a significant change in the contact angle of water on pre-stretched Teflon about a certain threshold in the

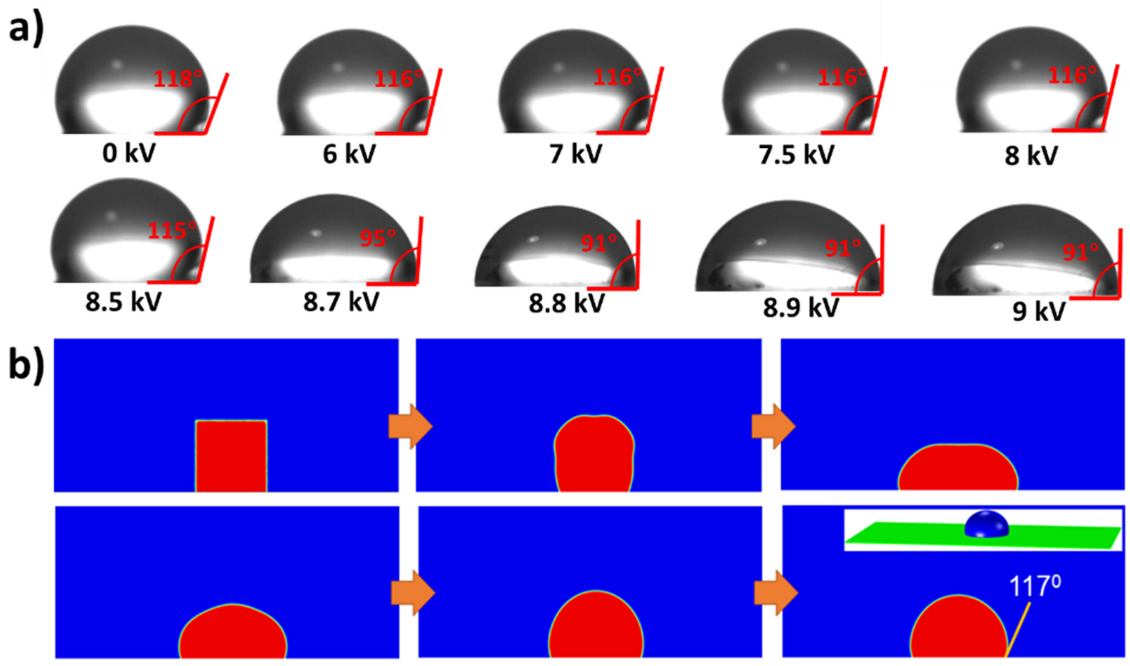

FIG. 2. (a) Equilibrium contact angle of water on the 25% pre-stretched Teflon specimen observed experimentally at different applied voltages. The positive high voltage is applied on the right-hand side. (b) The CHNS calculation results for the drop evolution toward the equilibrium static shape. No voltage is applied in the simulations.

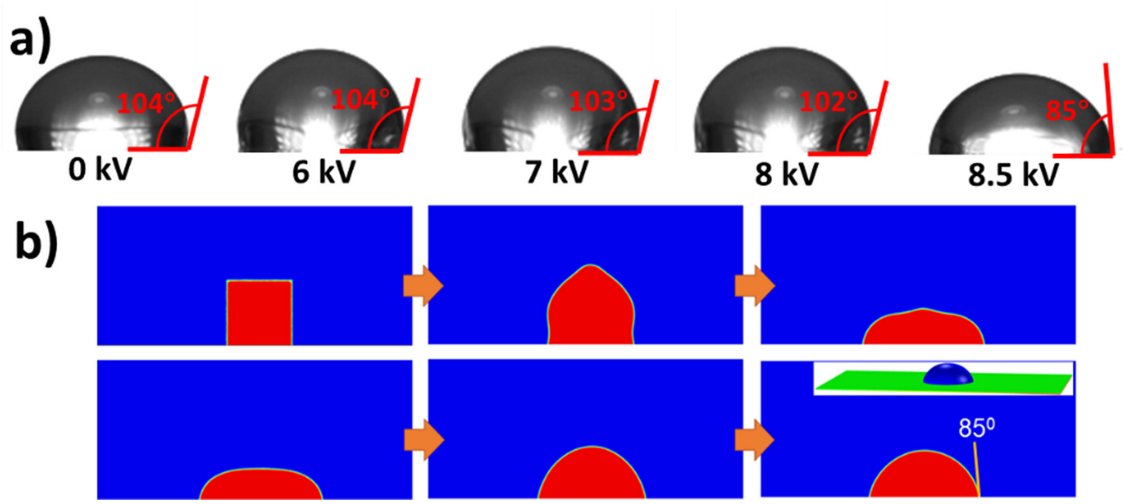

FIG. 3. (a) Equilibrium contact angle of water on the 50% pre-stretched Teflon specimen observed experimentally at different applied voltages. The positive high voltage is applied on the right-hand side. (b) The CHNS calculation results for the drop evolution toward the equilibrium static shape. The 8.5 kV voltage is applied in the simulations.

applied voltage. Typically, the applied voltage of 7.5–10 kV triggered the change for similar Teflon specimens at the electrode separation of 1.5 cm.

The observations of the static contact angle of water on the unstretched Teflon did not reveal any measurable changes in the entire voltage range below the corona discharge (spark) voltage (∼11 kV for the 1.5 cm electrode separation). The formation of sparks was undesirable. Spark formation was not observed in Ref. 21, probably because of the different thickness of the Teflon membrane and also possibly due to the differences in surface features.

Figure 2(b) shows the simulation results for 0 V, with the contact angle value on the 25%-stretched Teflon given for the longitudinal median cross-section of the 3D drop. The inset in the last image depicts the predicted full 3D view of a water drop on Teflon surface. As can be seen in Fig. 2(b), the predicted equilibrium contact angle is $117° \pm 2°$, in good agreement with the experimental measurements shown in Fig. 2(a) (the first image).

It is observed in the experiments that the application of a high voltage to the bottom of the Teflon surface changes the static contact angle of a sessile drop on top of the Teflon specimen. In the simulations 8.5 kV is applied on one side of the 50%-stretched Teflon, while keeping 0 V on the other side. The distance between the electrodes is 1.5 cm, the same as in the experiments. Figure 3(b) depicts the results for the predicted drop shape at 8.5 kV, similarly to Fig. 2(b). The predicted contact angle in the longitudinal median cross-section is $85° \pm 2°$, which is in good agreement with our experimental measurements [Fig. 3(a), the last image].

The recorded equilibrium contact angles of water drops at different applied voltages on parafilm are displayed in Fig. 4(a). In contrast to the abrupt change on Teflon, the contact angle was found to gradually decrease as the applied voltage increased. The contact angle decreased from 105° at 0 kV to 84° at 9 kV. We have further performed static contact angle calculations for parafilm at 9 kV. The CHNS predictions are shown in Fig. 4(b). The predicted static contact angle is in very good agreement with the experimental data in Fig. 4(a) (the last image).

B. Water drop impact onto parafilm

At water drop impact velocity of 1.44 m/s, 10/10 trials resulted in drop rebound on parafilm substrate without application of voltage. A trial, which demonstrates a typical behavior, is illustrated in Fig. 5. It should be emphasized that there were some deviations from the typical behavior, which were observed in some of the trials. For example, a few cases revealed not immediately merging drops in contact during the recoil stage (cf. Fig. 5, the frames from t + 48 ms to t + 56 ms). A plausible explanation of a delayed droplet coalescence would be the following one. Pressure in the air layer between too closely approaching droplets increases to that extent that air dissolution in water (governed by Henry's law) increases to that extent that the surface layer is so significantly enriched by air, that surface tension decreases locally near the closest approach location. As a result, water is pulled from that location in both droplets by the surface tension which stays high away from that location, and droplet coalescence is delayed. This is essentially a variant of the Marangoni effect associated in this case with air being an admixture. Such a situation is reminiscent of the "walking droplets" observed in the case of drop bouncing from a bath of liquid.[38,39] A further future work is needed to check the validity of this explanation.

The application of 9 kV voltage revealed no rebound in all the 10 consecutive trials performed. The corresponding features observed during water drop impact onto parafilm with the voltage applied are presented in Fig. 6. The results reveal some geometric features appearing during the drop retraction stage after the impact as observed in top and side views in Fig. 6, which demonstrate receding breakup of the main drop. The initial time moments from t to t + 6 ms show the lamella stretching due to the applied electric field. It should be emphasized that the retraction is slowed down considerably due to the electric field and the lamella appears to be pinned at some points along its perimeter. This pinning effect leads to finger formation (t + 4 ms) resulting in the formation of the secondary droplets on the substrate surface as is seen at t + 6 and t + 8 ms. In cases with the applied voltage, an additional dimensionless group of relevance is the electric Bond

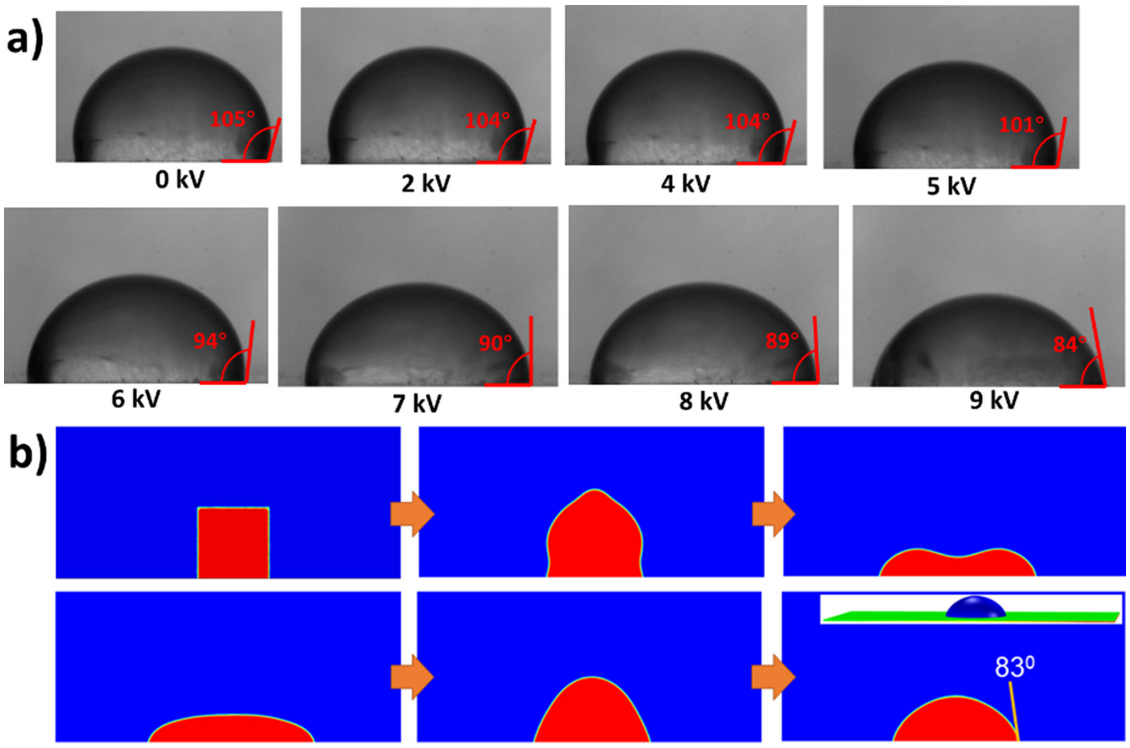

FIG. 4. (a) Equilibrium contact angle of water on a parafilm specimen observed experimentally at different applied voltages. The positive high voltage is applied on the right-hand side. (b) The CHNS calculation results for the drop evolution toward the equilibrium static shape. The 9 kV voltage is applied in the simulations.

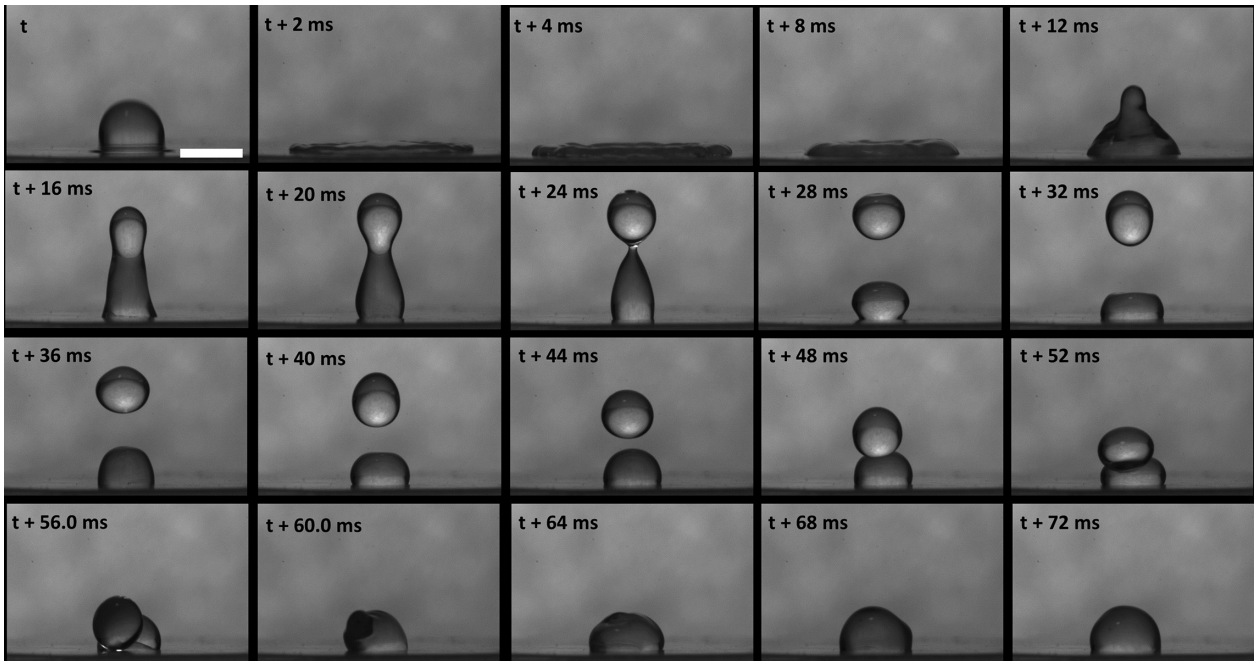

FIG. 5. Snapshots of water drop impact onto a parafilm substrate. The average drop diameter is 2.5 mm, the inter-electrode distance is 1.5 cm, the average velocity of drop impact is 1.44 m/s, and the acquisition frame rate is 2000 fps. Scale bar is 2 mm. The Weber number We = 72.0, the Ohnesorge number Oh = 0.002, and the composite parameter (relevant to splashing) K = 864.8. Here and hereinafter, t is the moment of the drop impact.

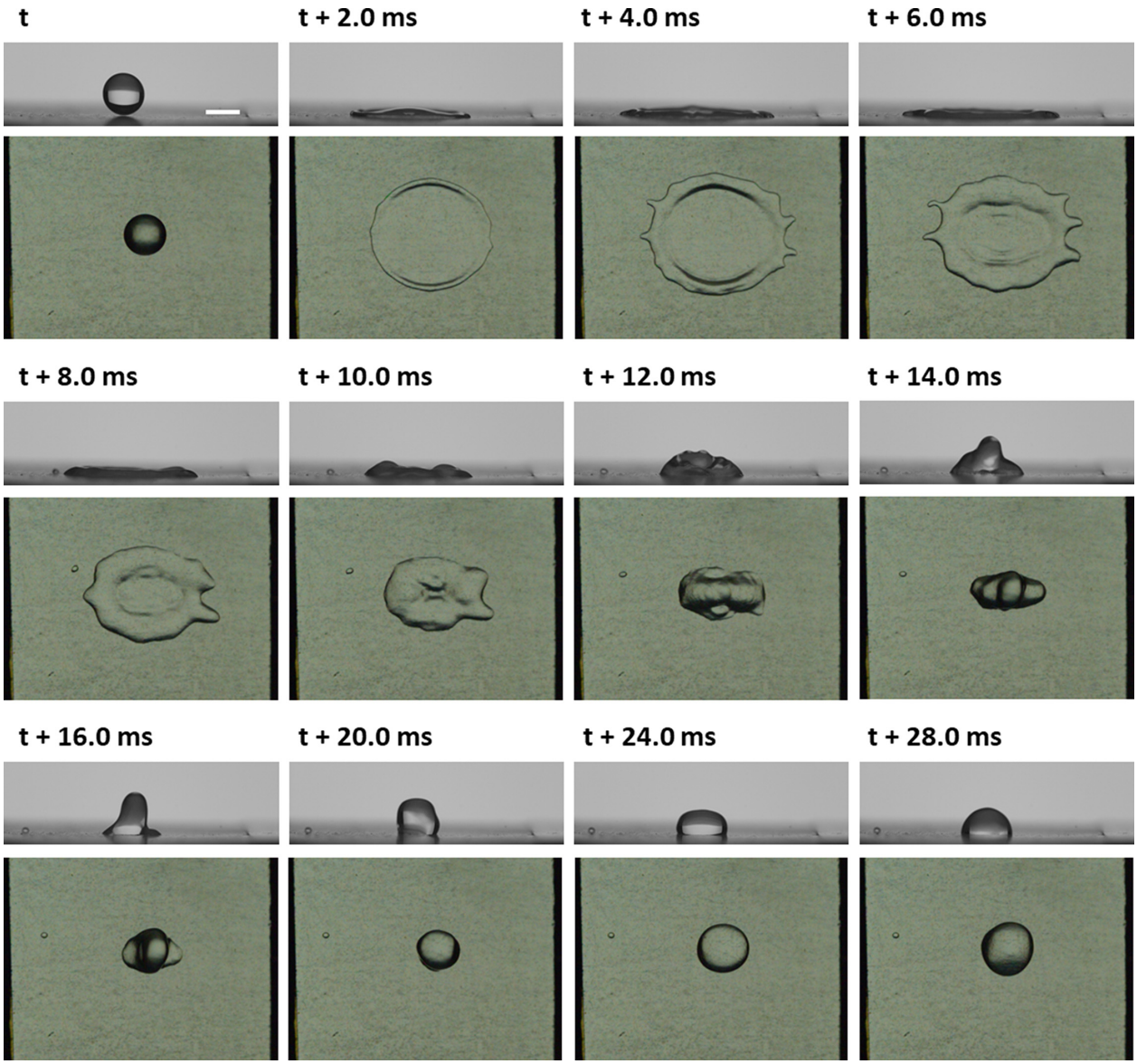

FIG. 6. Snapshots of water drop impact onto a parafilm substrate with the voltage of 9 kV applied (the electric field strength of 6×10^5 V/m). Rows 1 and 2: the side and top views, respectively, through the time moments t to t + 6 ms (with t being the moment of the drop impact). Rows 3 and 4: the side and top views, respectively, through the time moments t + 8 ms to t + 14 ms. Rows 5 and 6: the side and top views, respectively, through the time moments t + 16 ms to t + 28 ms. The average drop diameter is 2.5 mm. The average impact velocity is 1.44 m/s. The acquisition frame rate is 2000 fps. Scale bar is 2 mm. The dimensionless groups are We = 72.0, Oh = 0.002, K = 864.8, and $Bo_E = 1.4$.

number[2] $Bo_E = DE^2/\gamma$, where E is the applied electric field strength between the electrodes. In the present case, $Bo_E = 1.2$. A similar behavior was observed with application of 8.5 kV voltage, with the corresponding results being presented in SI (Fig. S4).

Further preliminary results were obtained at the dripping height of 65 cm, which resulted in an average velocity of drop impact of 3.16 m/s (cf. Fig. S5 in SI). The results presented in Fig. S5 in SI at such high impact velocities indicate the effectiveness of the application of the electric field even in such cases. For numerical simulations, it is desirable to consider lower impact velocities. This is because the high impact velocity and strong thinning of the spreading lamellae necessitate prohibitively small cell size in the numerical implementation. Accordingly, here the focus is on moderately high impact velocities only.

To better understand the dynamics of water drop impact onto a solid hydrophobic surface, we have performed CHNS simulations related to the experimental results presented above in this sub-section. We first investigated the drop impact on a dry solid parafilm surface

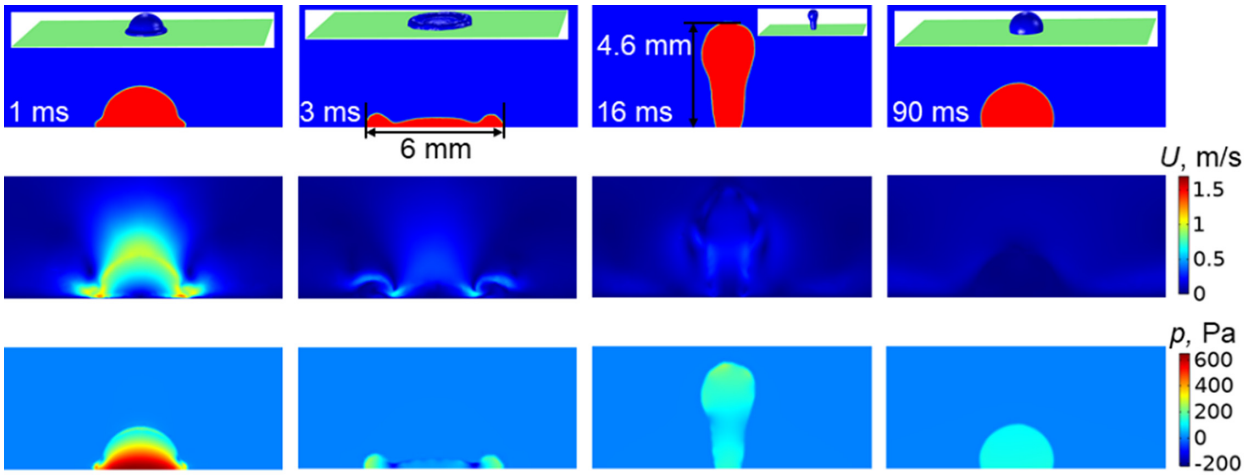

FIG. 7. The predicted drop evolution (the upper panel), with red color being the water drop and blue color being air during the impact onto a parafilm surface. The velocity magnitude (the second panel) and the pressure field during the impact (the lower panel). The drop diameter is 2.5 mm, and the initial drop velocity is 1.44 m/s.

without the applied voltage. The modeling results regarding the impact, spreading and rebound of water drop on parafilm surface are presented in Fig. 7. The upper panel in this figure depicts the evolution of the drop shape in time, with the red color representing the water drop and blue color corresponding to the gas phase (air). In addition, the small inset shows a full 3D view of the water drop on parafilm. The second panel in Fig. 7 depicts the velocity magnitude, whereas the third row shows the pressure field during the impact. The results were directly compared to our experimental results shown in Fig. 5 in terms of the spreading distance (s_{max}) and the maximum rebound height (h_{max}). In particular, the predicted maximum spreading distance, reached at the time moment of 3 ms, is equal to 6 mm compared to 6.3 mm observed in the experiment. The maximum rebound height observed in the experiments was 4.5 mm vs the prediction of 4.6 mm. The numerical predictions revealed that the spreading lamella bumps up as a rim, which is typical of the experimental observations. Thus, we can conclude that the present modeling results of the drop impact on parafilm surface without the applied voltage match the experimental results well.

Analyzing the velocity magnitude presented in the middle panel in Fig. 7, one observes the highest values (~1.6 m/s) corresponding to the initial moment of the drop impact onto the surface, as expected. The velocity magnitude decays significantly as the drop spreads and rebounds off the surface. A significant pressure increase is predicted at the drop bottom at the initial moments. Then, pressure diminishes at the later stages. A significant pressure increase and the nature of the pseudo-body force distribution (the numerically implemented surface tension) result in a relatively high drop rebound height.

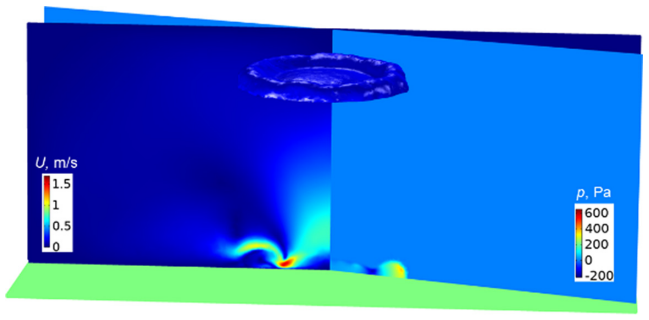

FIG. 8. Predicted 3D isometric view of the drop at the time moment of 3 ms accompanied by the results for the velocity magnitude, pressure, and the drop shape.

Figure 8 shows a full 3D isometric view of the drop of Fig. 7 at the time moment of 3 ms (when the maximum spreading has been reached). It also visualizes velocity magnitude, pressure field and the drop profile. A typical rim attached to a very thin water lamella in the middle is predicted, which is in good agreement with the experiment in Fig. 5.

Water drop impact onto a polarized parafilm surface predicted at the 9 kV applied voltage is presented in Fig. 9. These results agree with the corresponding experimental data in Fig. 6 in terms of the maximum spreading and rebound height. Specifically, the predicted maximum spreading diameter reaches about 8 mm compared to 8.7 mm in the experiment, and the predicted 1.7 mm rebound height compares to 1.9 mm in the experiment.

Comparing the experimental and modeling results with and without the applied voltage, one can conclude that the applied voltage changes wettability of the substrate, while velocities and pressure remain similar. These modeling findings suggest that the application of the voltage as high as 9 kV does not change the properties of the liquid. The electrowetting should be beneficial for other liquids including those used for painting and coating.

C. Water drop impact onto Teflon

The impact tests were conducted with the 50% pre-stretched substrate at the water drop impact height of 11.5 cm, which resulted in the impact velocity of 1.44 m/s. Here, without any applied voltage, 10/10 tests resulted in drop bouncing off. Of them, two trials revealed complete rebound after the impact on the substrate and the remaining 8 trials revealed a partial rebound. On the other hand, with the application of 9 kV, none of the trials exhibited drop rebound. This clearly

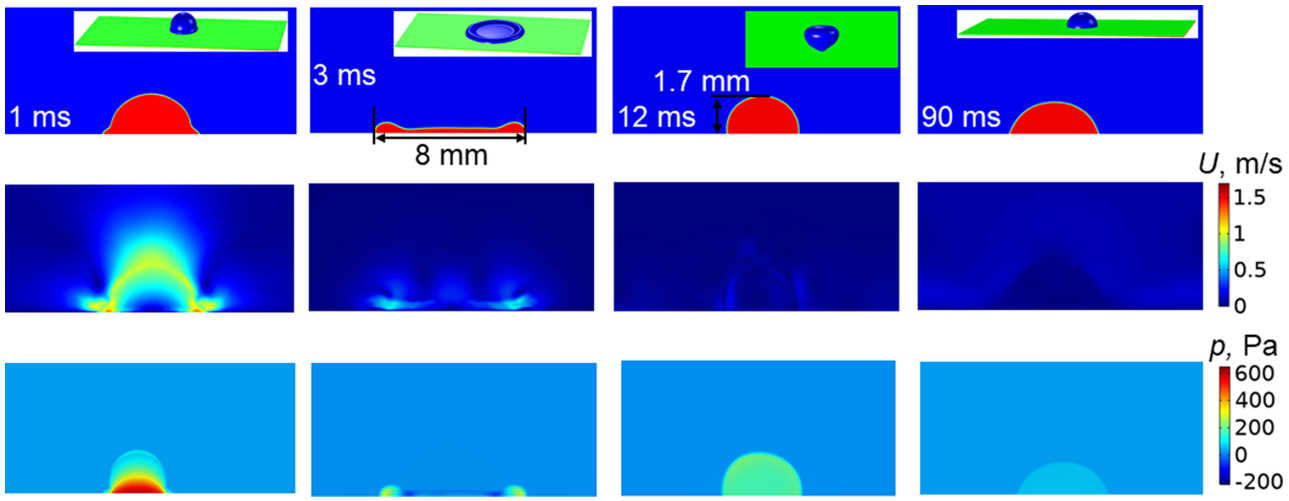

FIG. 9. CHNS modeling results for water drop impact onto a parafilm surface with the 9 kV applied voltage. The predicted drop evolution is shown in the upper panel, with red color corresponding to the water drop and blue color corresponding to air. The velocity magnitude is illustrated in the second panel, and the pressure field during the impact in the lower panel. The drop diameter is 2.5 mm, and the initial drop velocity is 1.44 m/s.

shows the suppressive effect of the applied electric field on the rebound, similarly to the previously considered cases of drop impact onto parafilm substrates.

Figure 10 illustrates the side and top views recorded during evolution of the drop during impact with no applied voltage and with the 9 kV voltage applied. Drop stretching by the electric field potentially leads to formation of fingerlike features during drop receding motion. The subsequent (to Fig. 10) time instances illustrated in Fig. 11 reveal the side views, which demonstrate drop rebound with no voltage and the rebound suppression due to the applied voltage.

Several preliminary experiments were also conducted at 8.5 kV for the 50% pre-stretched Teflon at the drop impact velocity of 3.16 m/s. However, some of the trials resulted in a spark close to the time of maximum spreading of the impacting drop. It should be emphasized that in the static experiment used for the contact angle measurement, no sparking was observed below 11 kV. This indicates a possible arcing between the spreading drop and the electrode. Hence, the maximum applied voltage that can be safely applied might be a function of the maximum drop spreading (and hence, the drop impact velocity) and the applied voltage. This is an important observation, which calls for an additional study, especially in the case of insulation at high voltages.[40] In the present work, the sparking regimes are avoided. The experimental results with the 8 kV applied voltage to the 50%-stretched Teflon specimen are presented in Fig. S6 in SI.

One of the important features to analyze is the drop footprint evolution following the drop impact. The footprint evolution of the impacted drop was traced using the results for water drop impact at the velocity of 1.32 m/s onto the 25% pre-stretched Teflon substrate; cf. SI (Figs. S7 and S8). The evolution of the footprint envelope obtained from the top view (Fig. S7 in SI) with and without application of 8.5 kV voltage is depicted in Fig. 12. The centers of the drops analyzed are very close in the cases presented, with an offset of only a few pixels in the images. It should be emphasized that due to a low contrast between the drop and the background, it is unclear whether the substrate surface could be really de-wetted around the footprint center during drop spreading. The electric force enhances spreading, which manifests itself as an increase in the spreading envelope, which appears to be stretched along the X axis in Fig. 13. Note that the effective envelope radius is determined via the envelope area S as $\sqrt{S/\pi}$. Note also that the increase in the footprint area reveals the flow component in the direction normal to the substrate.

The envelope evolution in the case of 8.5 kV is analyzed in time in Fig. 13(a). The comparison of the effective radius of the envelope without and with voltage is done in Fig. 13(b). Figure 13(a) reveals that the spreading is affected by the electric field, which also triggers some proto-fingerlike features. An increase in the effective radius due to the applied voltage is clearly seen in Fig. 13(b). The time moment t + 3.0 ms corresponds to the maximal spreading along the Y (vertical)-axis [cf. Fig. 13(a)]. After that, the footprint begins retracting through the time moments from t + 4.0 ms to t + 5.0 ms. However, along the X-axis, the envelope appears to be pinned at certain locations, while still spreading at some other locations around the proto-fingerlike features (at t + 4.0 ms). This competition of stretching and receding is also reflected by the corresponding plateau in the dependence of the effective radius on time in the case with the applied voltage [Fig. 13(b)].

Similarly to the case of drop impact onto the parafilm surface, we have performed PFM calculations of the drop impact onto Teflon surface. Figure 14 shows the CHNS predictions of the drop impact, spreading and rebounding off the 50%-stretched Teflon surface (0.081 mm thick) at the 9 kV applied voltage. Red color in the upper panel depicts the drop shape evolution, and blue color shows the gas phase (air). The thin green layer at the bottom in the insets with the isometric views of the impacting drop depicts Teflon dielectric layer, where the potential difference between 0 kV and 9 kV is applied. The second panel in Fig. 14 shows velocity magnitude, whereas the last one presents the pressure field during the impact. The maximum spreading distance of 6.9 mm and the maximum rebound height of 2.0 mm were predicted. The predicted drop shape evolution during the impact is in good agreement with the experimentally observed one (cf. Fig. 10). In particular, the experiment (cf. Fig. 10) reveals the

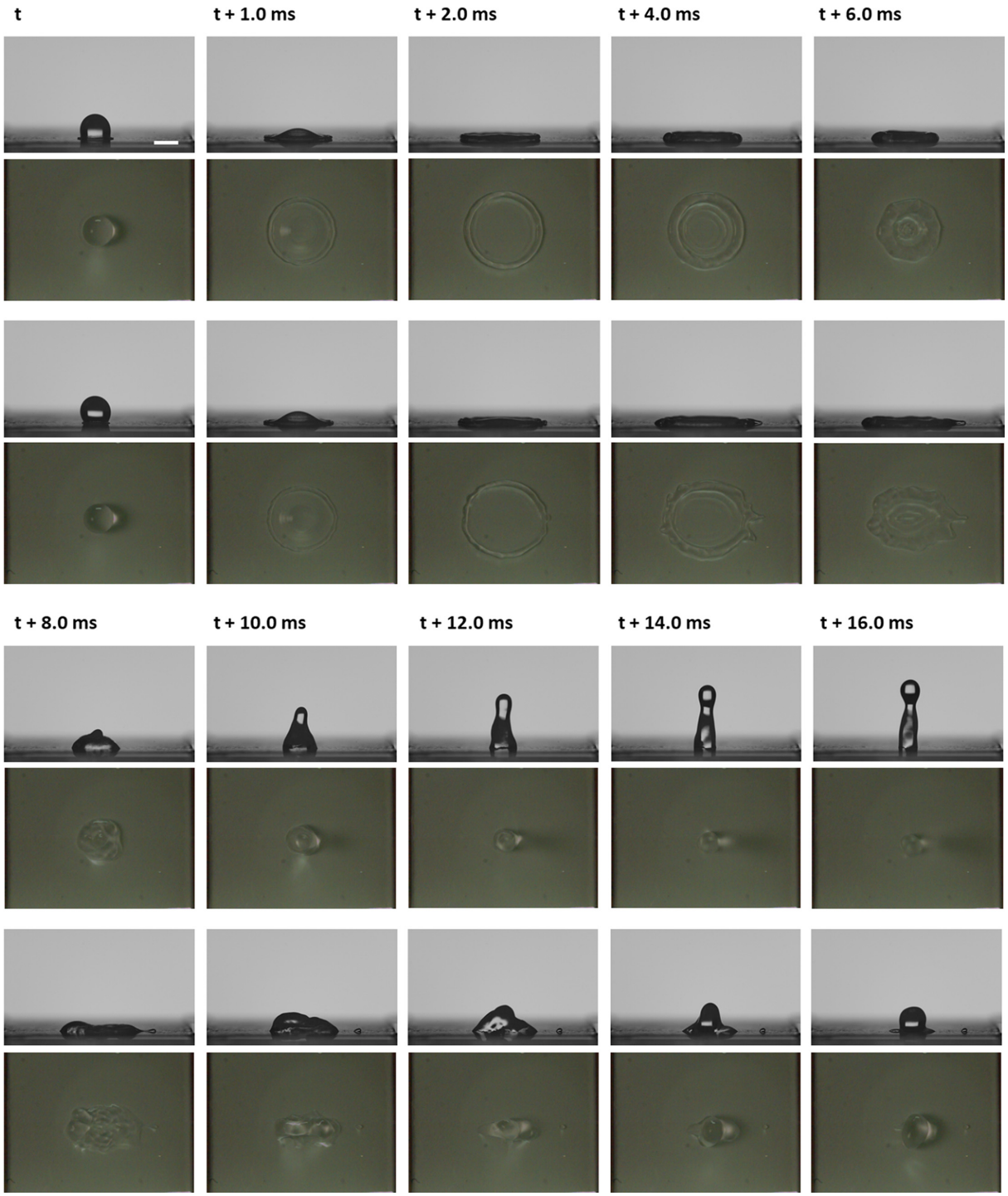

FIG. 10. Snapshots of water drop impact onto the 50% pre-stretched Teflon substrate. Rows 1 and 2: no applied voltage; the side and top views, respectively, through the time moments t to t + 6 ms (with t being the moment of drop impact). Rows 3 and 4: 9 kV applied voltage; the side and top views, respectively, through the time moments t to t + 6 ms. Rows 5 and 6: no applied voltage; the side and top views, respectively, through the time moments t + 8 to t + 16 ms. Rows 7 and 8: 9 kV applied voltage; the side and top views, respectively, through the time moments t + 8 to t + 16 ms. The average initial diameter of the drops is 2.5 mm. The inter-electrode distance is 1.5 cm. The 9 kV voltage is applied to the right-hand side electrode. The average velocity of drop impact is 1.44 m/s. The acquisition frame rate is 2000 fps. Scale bar is 2 mm. The dimensionless groups are We = 72.0, Oh = 0.002, K = 864.8, and $Bo_E = 1.4$.

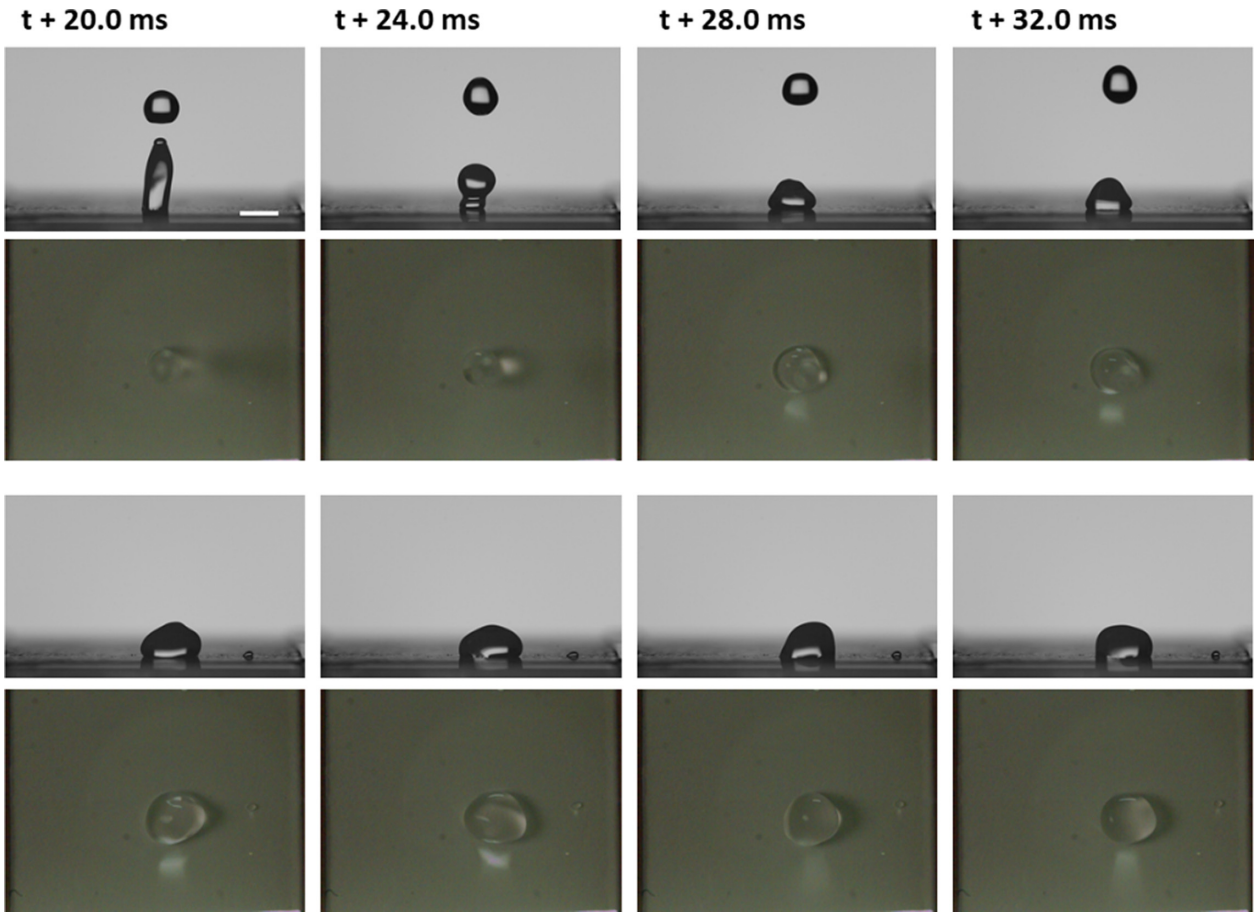

FIG. 11. Snapshots of the side views of the water drop impact (subsequent to the snapshots shown in Fig. 10) onto the 50% pre-stretched Teflon substrate. Rows 1 and 2: no applied voltage, through the time moments from t + 20 to t + 32 ms (with t being the drop impact moment). Rows 3 and 4: 9 kV applied voltage (the electric field strength of 6×10^5 V/m) through the time moments from t + 20 to t + 32 ms. The average drop diameter is 2.5 mm. The inter-electrode distance is 1.5 cm. The 9 kV voltage is applied to the right-hand side electrode. The average velocity of drop impact is 1.44 m/s. The acquisition frame rate is 2000 fps. Scale bar is 2 mm. The dimensionless groups are We = 72.0, Oh = 0.002, K = 864.8, and $Bo_E = 1.4$.

maximum spreading distance of 7.6 mm at the time moment t + 4 ms and the maximum rebound height of 2.3 mm at the time moment t + 15 ms. Analyzing the velocity magnitude presented in the middle panel of Fig. 14, one observes the highest values (1.6 m/s) corresponding to the initial moments of the drop impact onto the surface, as expected. The velocity magnitude decays significantly as the drop spreads and rebounds off the surface. A significant pressure increase can be observed at the bottom of the drop at the initial impact

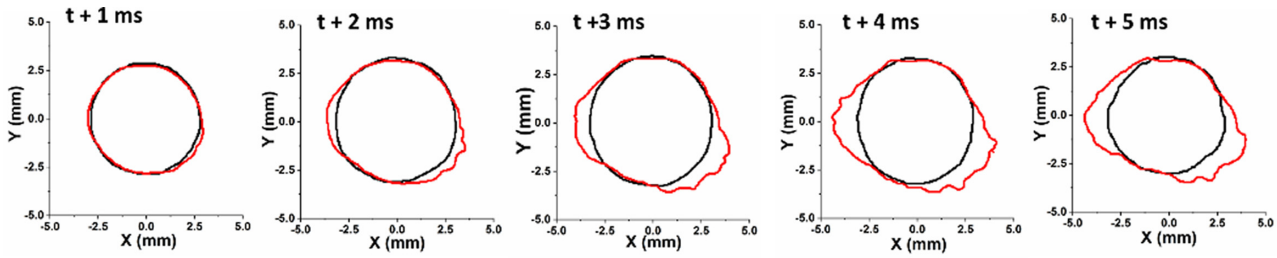

FIG. 12. Evolution of the water drop footprint envelope during spreading on the substrate after an impact at the moment t as observed experimentally in the top view. Black line corresponds to the case of no applied voltage, while red line to the case of 8.5 kV applied voltage (the electric field strength of 5.67×10^5 V/m). The +8.5 kV electrode is applied on the right-hand side, while the grounded electrode is on the left.

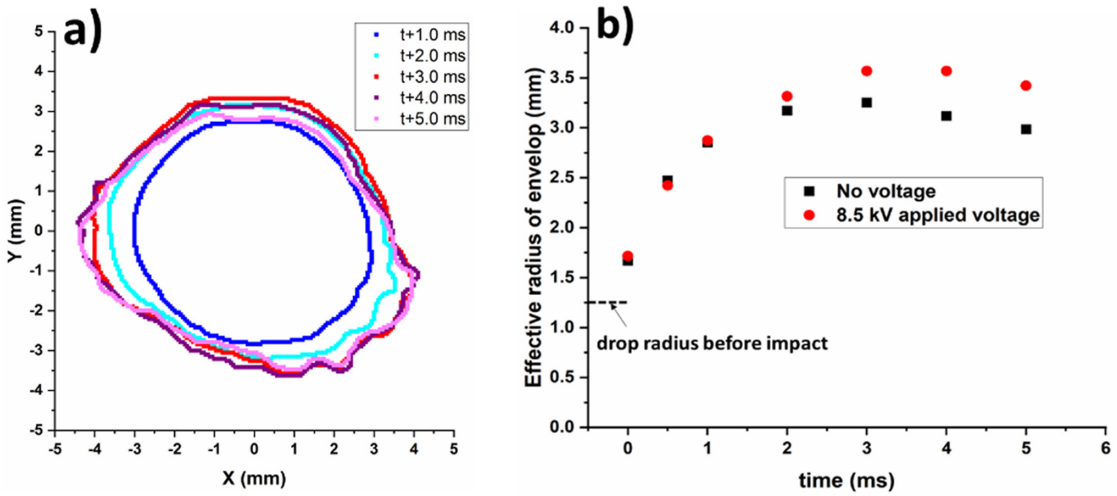

FIG. 13. (a) Evolution of the water drop envelope footprint during spreading on the substrate after the impact at time t. The case of 8.5 kV applied voltage (the electric field strength of 5.67×10^5 V/m). (b) The effective radius of the envelope vs time. The +8.5 kV electrode is applied on the right-hand side, while the grounded electrode is on the left.

moments, which changes to a relatively uniform pressure distribution at the later stages.

Analyzing the modeling results of the drop impact onto the parafilm and Teflon surfaces, one can conclude that the applied voltage facilitates the electrowetting on both materials. The latter affects drop spreading and diminishes/suppresses bouncing off from the surface.

D. Water drop impact onto polypropylene

Water drop impact onto a polypropylene substrate with the impact velocity of 1.44 m/s did not reveal any rebound. Five trials were conducted with and without applied voltage and they revealed a similar behavior. The representative trial with no applied voltage is illustrated in Fig. 15. This result corresponds to the partial hydrophobicity of polypropylene substrates. Furthermore, with the applied voltage of 8.5 kV, the results reveal the lamella stretching in the direction of the electric field (cf. Fig. 16) similarly to the Teflon and parafilm substrates. The stretching results in formation of small fingers protruding toward the electrodes, and one of them left a small secondary droplet during the receding stage.

E. N-butanol drop impact onto polypropylene

The experimental results for the n-butanol drop impact onto polypropylene are shown in Figs. 17 and 18. The average velocity of the drop impact was 2.50 m/s, which results in the prompt splashing.

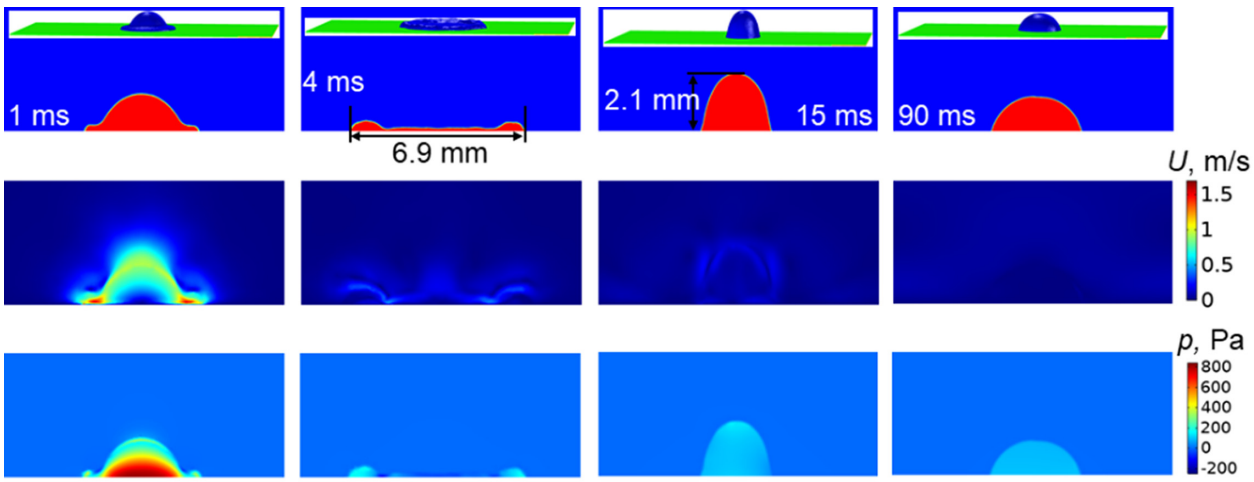

FIG. 14. CHNS predictions for water drop impact onto the 50%-stretched Teflon surface with the 9 kV applied voltage. The predicted drop evolution (the upper panel), with red color being the water drop and blue color being air. Velocity magnitude (the second panel) and the pressure field during the impact (the lower panel). The drop diameter is 2.5 mm, and the initial drop velocity is 1.44 m/s.

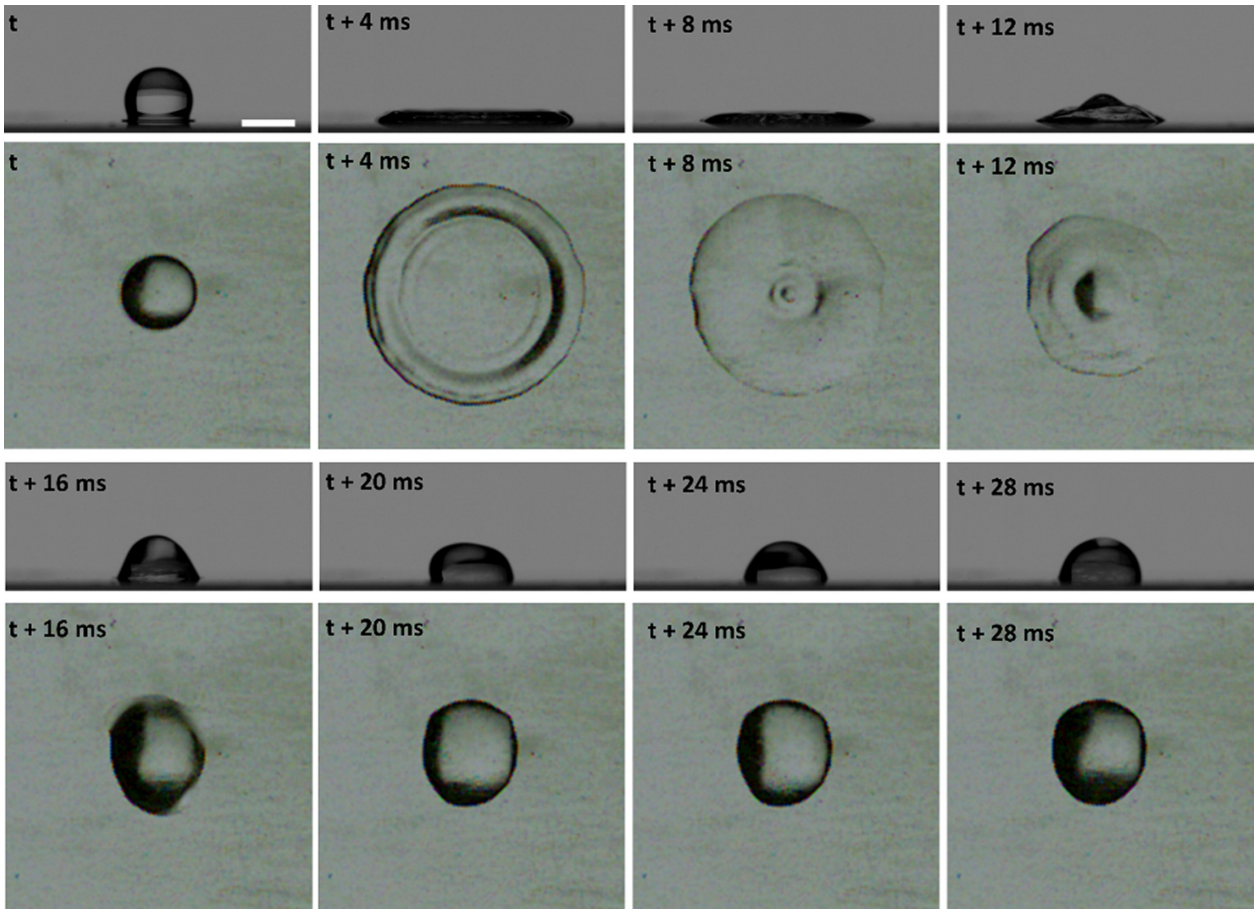

FIG. 15. Snapshots of water drop impact onto a polypropylene substrate without electric field applied. Rows 1 and 2: the side and top views, respectively, through the time moments t to t + 12 ms (with t being the moment of drop impact). Rows 3 and 4: the side and top views, respectively, through the time moments t + 16 ms to t + 28 ms. Scale bar is 2 mm. The top- and side-view cameras are synchronized with the acquisition frame rate of 2000 fps. The dimensionless groups are We = 72.0, Oh = 0.002, and K = 864.8.

The splashing with many secondary droplets is clearly visible in both the top and side views in Figs. 17 and 18, respectively. These results were obtained with the 8.5 kV voltage applied.

The cases without applied voltage consistently revealed prompt splashing in all azimuthal directions with 28–35 secondary droplets ejected. In contrast, when voltage has been applied, the total number of secondary droplets reduced to 13–18. The count is based on the visualization of 5 trials, as observed in the top view. It should be emphasized that in the present case at the resolution of 29 μm/pixel (top view), smaller secondary droplets reported in prompt splashing[41] would not be visible. In the case of n-butanol drop, the values of K = 2153.1 and We = 379 can be compared to K = 864.8 and We = 72 for water drop with the impact velocity of 1.44 m/s considered above. However, the water drop impact with the velocity of 3.16 m/s (discussed in SI) reveals the values of K = 4167.9 (higher than K = 2153.1 for n-butanol) and We = 347, albeit such an impact did not result in any prompt splashing. This is in concert with the fact that the K-parameter alone could not predict the threshold to prompt splashing, and interfacial properties such as roughness and wettability also affect prompt splashing.[7,25]

Furthermore, it was noticed that with the electric field applied unique features could be observed. In particular, the dynamics of spreading depends on the azimuthal direction (cf. Fig. 17, the bottom row). In the direction perpendicular to the direction of the applied electric field (the vertical direction in Fig. 17), the prompt splashing was diminished, whereas in the direction of the electric field, the prompt splashing was suppressed (along the left and right arcs in Fig. 17, in the bottom row). Note also that there are no detached secondary droplets visible in or near the visualization plane in the side view (cf. Fig. 18, the right-hand side column). One can see the shades of secondary droplets (cf. Fig. 18, the right-hand side column) which fly toward and away from the plane of visualization, as expected for the droplets moving in the perpendicular direction seen in the top view (cf. Fig. 17, the bottom row). Furthermore, the lamella spreading was also significantly different toward the cathode vs the anode (cf. Fig. 17, top view). Toward the cathode (the grounded electrode), the spreading revealed the long finger formation (along the blue arc in

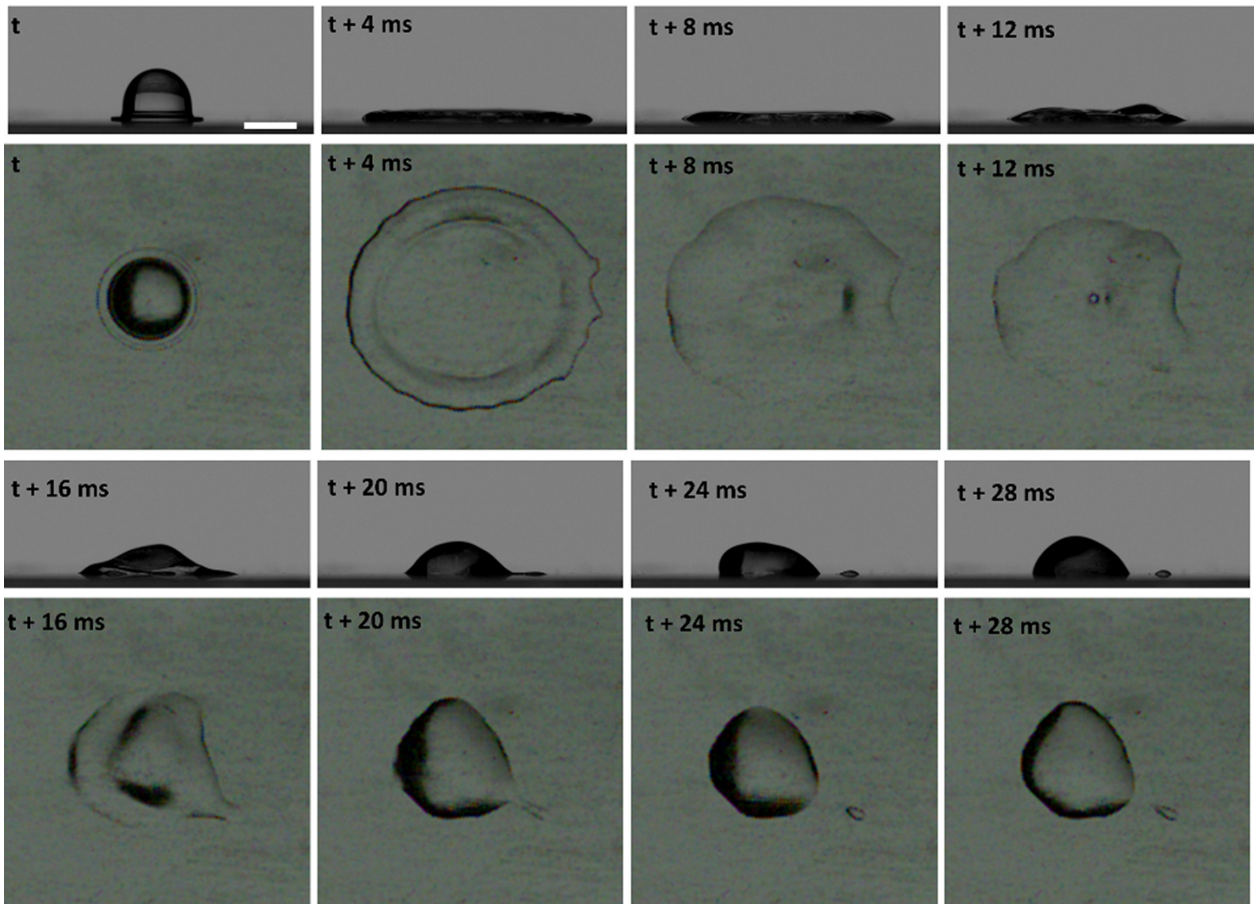

FIG. 16. Snapshots of water drop impact onto a polypropylene substrate with the 8.5 kV voltage applied (the electric field strength of 5.67×10^5 V/m). Rows 1 and 2: the side and top views, respectively, through the time moments t to t + 12 ms (with t being the moment of drop impact). Rows 3 and 4: the side and top views, respectively, through the time moments t + 16 ms to t + 28 ms. Scale bar is 2 mm. The right-hand side electrode is +8.5 kV (anode) and the left-hand side one is grounded (cathode). The top- and side-view cameras are synchronized with the acquisition frame rate of 2000 fps. The dimensionless groups are We = 72.0, Oh = 0.002, K = 864.8, and $Bo_E = 1.2$.

Fig. 17, the bottom row). However, most of these fingers did not detach from the primary drop and were eventually engulfed by the spreading rim. Toward the anode (where positive voltage was applied), the spreading n-butanol drop did not display any finger formation (along the green arc Fig. 17, bottom row).

The rim of the expanding drop in Fig. 17 reveals some color features. This could be attributed to rainbow-like formation due to the different refractive indices of different colors. The optical caustics structures depend on the local shape of liquid element and the number of refractions-reflections at the interface leading to secondary, tertiary, or higher-order rainbow formation.[42,43]

Air entrapment was observed near the rim of the spreading n-butanol drop in some cases with the applied voltage. The top view in one of such cases is shown in Fig. 19. It should be emphasized that such bubble entrapment is unlike the entrapment of a central bubble, i.e., this behavior is radically different from the "impact bubble" and "entrapped bubble" reported in Ref. 44. The entrapment of additional bubbles around the lamella rim observed here with the applied voltage is discussed in more detail below.

It can be observed from the comparison of the side views that at the time moment t the lamella is pulled to the right in the case of the applied voltage (in Fig. 18, the right-hand side column) compared to the case without the electric field (in Fig. 18, the left column). Furthermore, in the next frame at t + 0.5 ms with the applied voltage (cf. Fig. 18), the left side of the lamella has also underwent significant elongation, while still being intact and connected with the main drop.

Comparing the simultaneous side and top views in the present results, one can recognize lamella detachment from the surface. For prompt splash, one can observe secondary droplet formation from only the extended jets issued from the lamella spreading on the surface. The present results do not feature a typical corona splash, but rather remind splash with a short corona.[25]

The observed suppression of formation of secondary droplets in the direction of the electric field ascertains the importance of the air layer underneath the expanding liquid lamella. According to the observations in Ref. 45, splashing of any type appears when two simultaneous conditions are met—one of them being the formation of an ejected lamella which is detached from the substrate, and the second

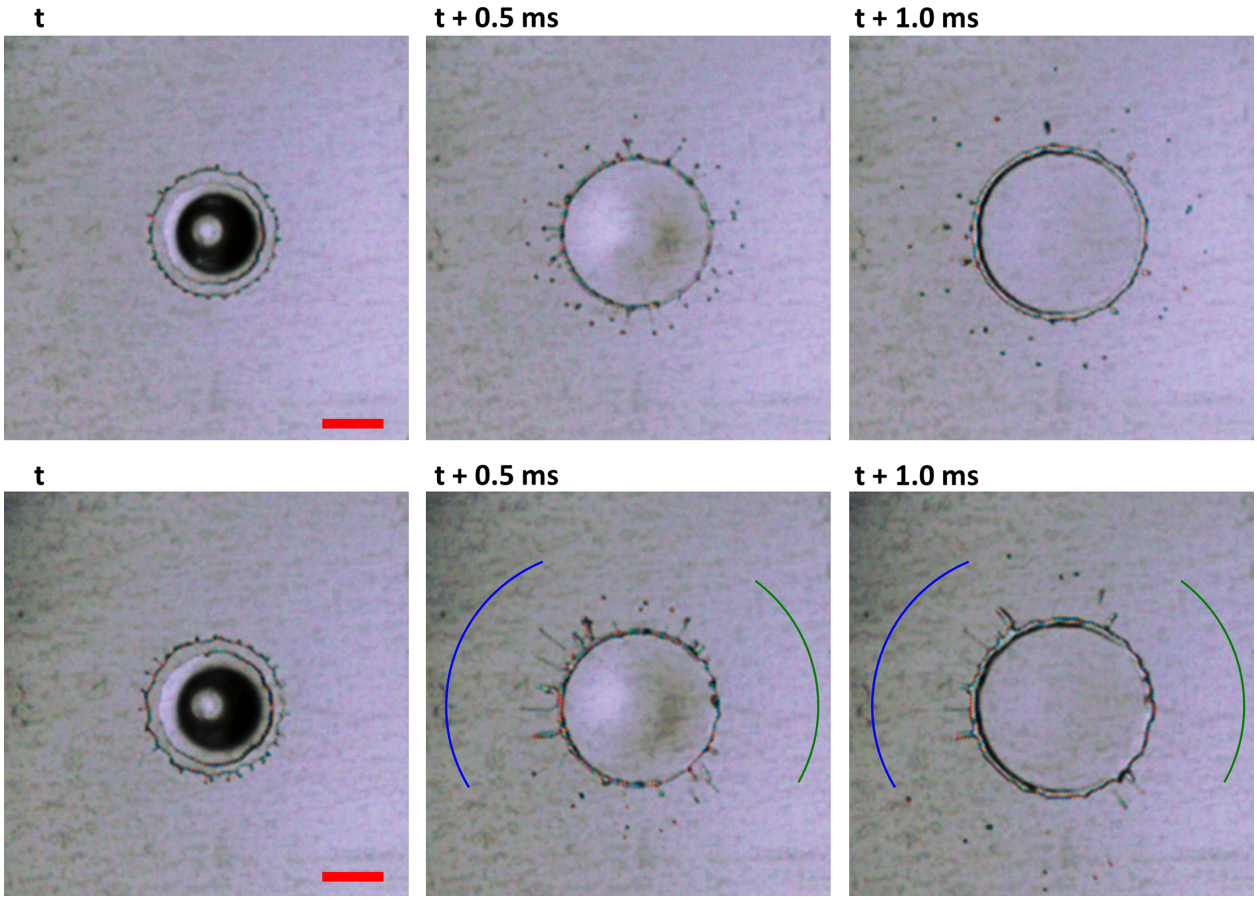

FIG. 17. Snapshots of the top view of n-butanol drop impact (the average diameter of 1.87 mm, the impact velocity of 2.50 m/s) onto a polypropylene substrate. Row 1: no applied voltage. Row 2: with the applied voltage of 8.5 kV (the electric field strength of 5.67×10^5 V/m); the right-hand side electrode is +8.5 kV (anode) and the left-hand side one is grounded (cathode). The blue arc indicates the direction where no splashing secondary droplets were observed, while fingers were seen. The green arc indicates the direction where neither splashing secondary droplets, nor fingers were observed. Scale bar is 2 mm. The top-view camera here and the side view camera (cf. Fig. 18) are synchronized with the acquisition frame rate of 2000 fps. The dimensionless groups are We = 379.0, Oh = 0.013, K = 2153.1, and $Bo_E = 2.7$.

one being the requirement that the lamella front possesses a sufficiently high vertical velocity to avoid rewetting.[45] The criterion for splashing relating the total lift force to the surface tension retraction is the so-called β parameter.[45] The parameter is defined as $\beta = \sqrt{F_L/2\gamma}$, where F_L is the lift force per unit length (in the direction perpendicular to the lamella cross-section: cf. the inset in Fig. 20), and γ is the surface tension of liquid. The critical value of β above which splashing was observed in many experiments was ~0.14.[25,45] In the present case, it can be assumed that the aerodynamic lift acting on the lamella is also opposed by the electric Coulomb force due to the ion redistribution in the liquid, as is schematically depicted in the inset in Fig. 20.

With the application of the electric field, the ions present in the initially electroneutral n-butanol drop are attracted to the electrodes with the opposite polarity. The charge relaxation time[2] expressed in the SI units is $\tau_c = \varepsilon\varepsilon_0/\sigma$ (where ε is relative dielectric constant of the liquid, ε_0 is the dielectric permittivity of vacuum, and σ is the electrical conductivity of the liquid). This is the characteristic timescale of the ion redistribution. For n-butanol[46,47] $\varepsilon \sim 18$ and $\sigma \sim 2 \times 10^{-6}$ S/cm, which yields $\tau_c \sim 1$ μs. This is significantly lower than the characteristic timescale of the prompt splashing (~0.1–1 ms). Hence, for all the time moments observed in the present experiments, the free charges are concentrated along the free surface according to the applied electric field, i.e., the drop behaves as a perfect conductor with the charge carriers concentrated at the free surface and screening the electric field inside liquid. Accordingly, the situation depicted in Fig. 20 arises. This electric force acting on the ions counteract the surface tension, which, otherwise, would facilitate a further deformation of the liquid surface. It is interesting to note that the drop side facing the positive electrode does not reveal too much deformation or finger formation. This can possibly be due to early wetting of the surface in combination with the lower mobility of anions compared to the cations. Moreover, this additional effect of the lamella attraction to the substrate caused by the applied voltage can result in the lamella impact onto the surface accompanied by bubble entrapment observed along the rim, as discussed previously in relation to Fig. 19.

Furthermore, without the applied voltage, there is no observed lamella spreading from 20 to 50 ms. On the other hand, the lamella

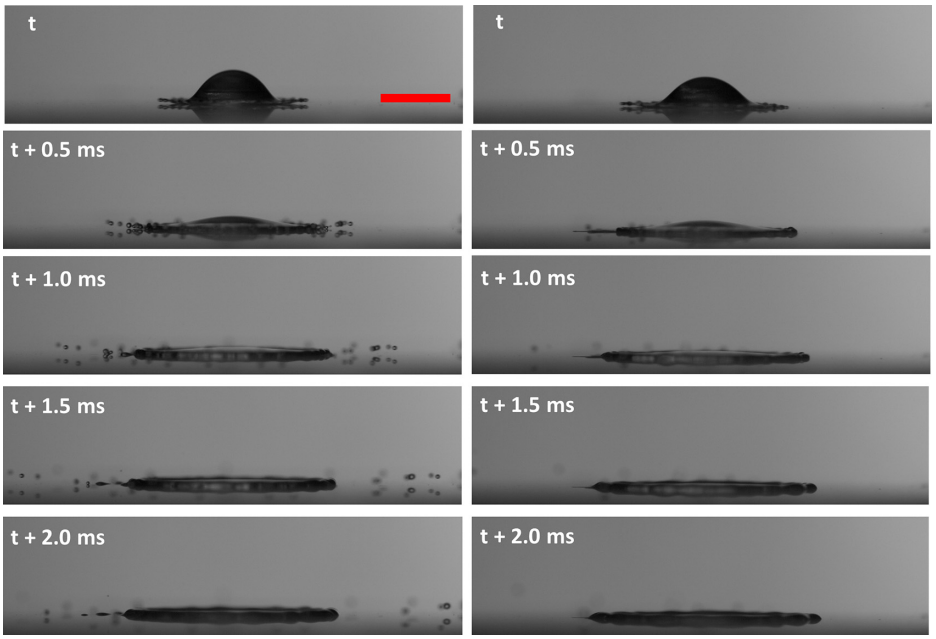

FIG. 18. Snapshots of the side view of n-butanol drop impact (the average diameter of 1.87 mm, the impact velocity of 2.50 m/s) onto a polypropylene substrate. Left column: no applied voltage. Right column: the applied voltage of 8.5 kV (the electric field strength of 5.67×10^5 V/m), the right-hand side electrode is +8.5 kV (anode) and the left-hand side one is grounded (cathode). Scale bar is 2 mm. The top-view camera (cf. Fig. 17) and the side-view camera here are synchronized with the acquisition frame rate of 2000 fps. The dimensionless groups are We = 379.0, Oh = 0.013, K = 2153.1, and $Bo_E = 2.7$.

spreading in the case with the electric field applied continues for several seconds, as is seen in Fig. 21. The drop profile seen from the side view reveals a gradual increase in size during the observation time. In the top view, the drop profile becomes nearly transparent, which makes it difficult to visualize it with a good contrast. However, an approximate area analysis can be done, and the result is shown in Fig. 22. It reveals the corresponding increase in the area of the drop spreading resulting in an increased effective radius of the envelope after voltage application. Furthermore, similarly to the side view, the effective area reveals a gradual increase in time with no signs of

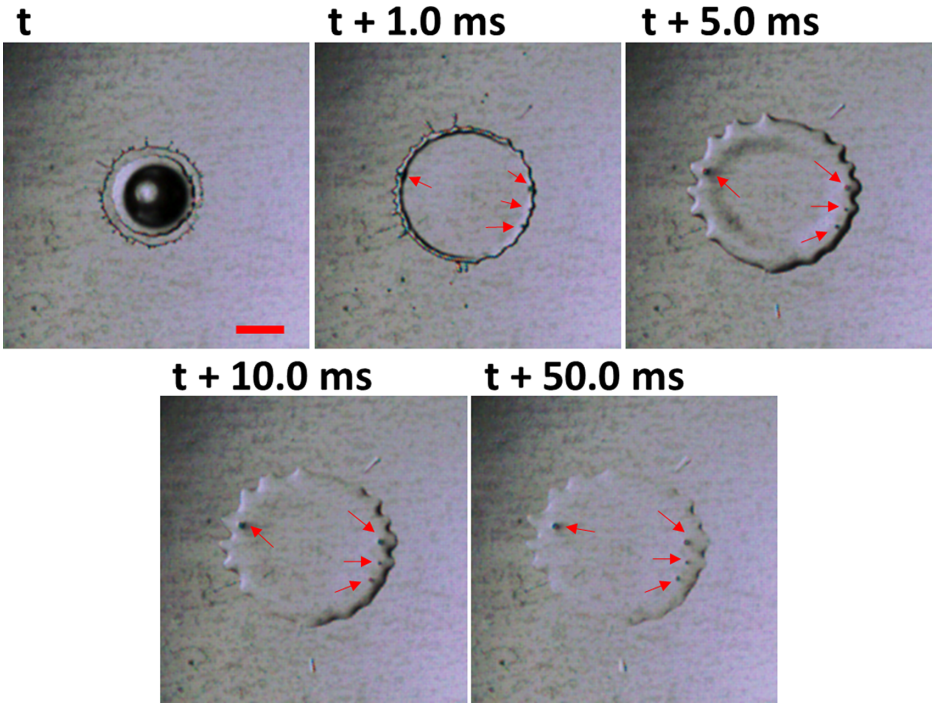

FIG. 19. Snapshots of the top view of n-butanol drop impact (the average diameter of 1.87 mm, the impact velocity of 2.50 m/s) onto a polypropylene substrate with the applied voltage of 8.5 kV (the electric field strength of 5.67×10^5 V/m). The red arrows indicate the entrapped air bubbles in the spreading lamella. Scale bar is 2 mm. The right-hand side electrode is at +8.5 kV (anode) and the left-hand side one is grounded (cathode). The acquisition frame rate is 2000 fps.

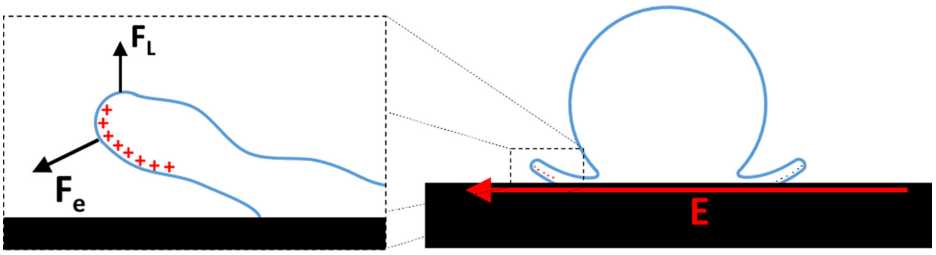

FIG. 20. Schematic of the drop impact with liquid lamella ejected during the initial phase and affected by the applied voltage (E is the electric field strength). The inset shows the expected charge redistribution along the lamella surface with an effective Coulomb force F_e acting toward the grounded electrode and counter-acting the lift force F_L.

saturation within the observation period. In contrast, without voltage being applied, the radius saturation was observed beyond 20 ms (cf. the inset in Fig. 22).

F. Motor oil drop impact on Teflon

The experiments with motor oil drop impact were conducted on the 25% pre-stretched Teflon substrate. The spreading dynamics was gradual with the contact angle changing slowly in time from t + 2 s to t + 3.5 s in cases without the electric field applied (cf. Fig. 23, the top row). The spreading was accelerated with the application of the 8.5 kV voltage as seen in Fig. 23 (the bottom row). Taking the relative dielectric constant of motor oil[48] ∼2.3 and electrical conductivity[49] ∼2 × 10^{-10} S/cm, the charge relaxation time of motor oil $\tau_c \sim 1$ ms. Further, viscosity of motor oil is relatively high[50] ∼50 cP, resulting in a slow evolution observed in Fig. 23.

The diminished contact angle in the case with the electric field applied (cf. the top and bottom rows in Fig. 23) reveals the electrowetting effect on the drop spreading.

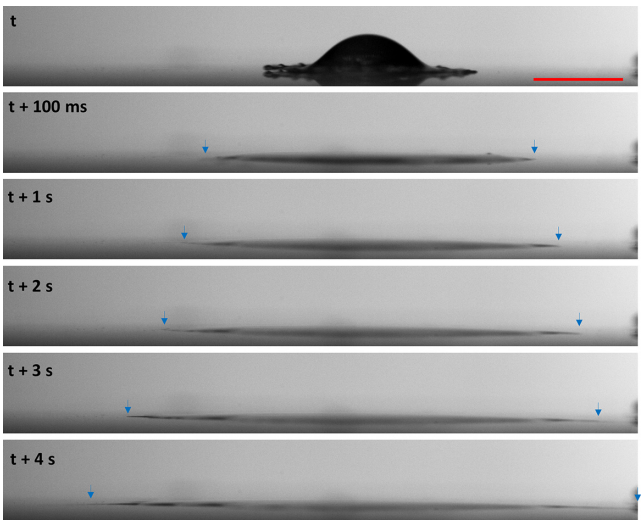

FIG. 21. Evolution of the n-butanol drop (the average diameter of 1.87 mm, the impact velocity of 2.50 m/s) spreading on a polypropylene substrate after the impact at time t with the 8.5 kV applied voltage. Blue arrows indicate the approximate position of the leading edge of the lamella front. The right-hand side electrode is at +8.5 kV (the anode) and the left-hand one is grounded (the cathode). The acquisition frame rate is 2000 fps.

IV. CONCLUSION

The dynamic evolution of drops impacting onto a dielectric substrate is in focus here, with the effect of the electric field on drop spreading being the main aim. Drop impacts of water, n-butanol, and motor oil were experimentally investigated onto different substrates—parafilm, pre-stetched Teflon, and polypropylene—with and without electric field applied. The experiments demonstrated that the electric field can significantly suppress drop rebound observed in the case of water.

The impact of water drops onto parafilm, pre-stretched Teflon, and polypropylene substrates was also modeled numerically by means of the phase-field model (PFM) using the Cahn–Hilliard–Navier–Stokes (CHNS) simulations. The predicted steady-state drop shapes on substrates without and with the applied voltage were in good agreement with the experimental observations. Moreover, the maximum spreading of water lamellae on the substrates was accurately predicted, as well in the case of drop bouncing, the bouncing height has been predicted in close agreement with the present experimental data.

With the application of the electric field, surface coverage by liquid can be enhanced for water and hydrocarbon liquids. In particular, the experiments demonstrated that in the case of drop impact of n-butanol, the results revealed a partial suppression of prompt

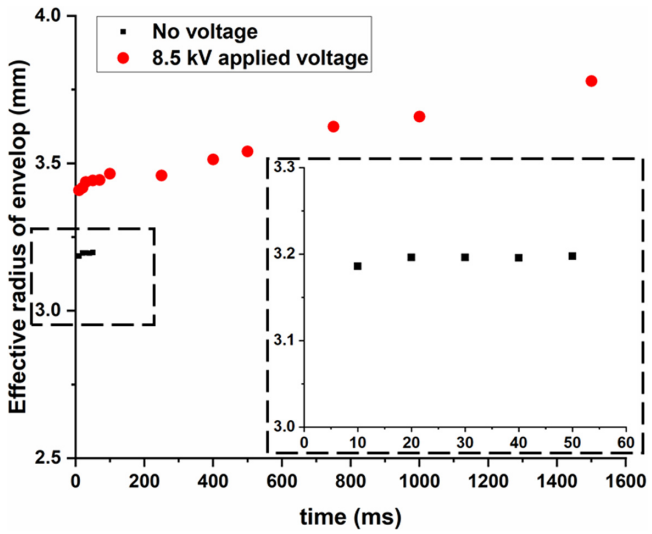

FIG. 22. Comparison of the effective radius of n-butanol drop obtained using the spreading envelope observed in the top view with and without the applied voltage. The inset shows the zoomed-in view in the case without voltage.

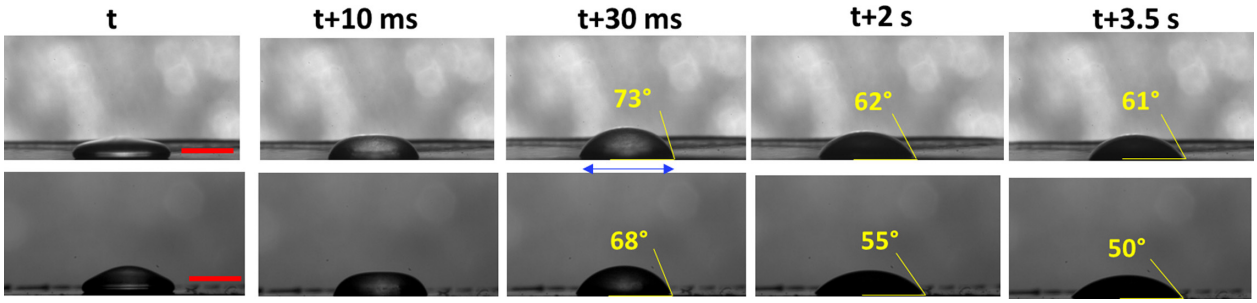

FIG. 23. Motor oil drop spreading on the 25% pre-stretched Teflon substrate. The average drop diameter is 2.40 mm, the impact velocity is 1.47 m/s. The drop impact happened at time t. Top row: no electric field applied, and bottom row: the applied voltage of 8.5 kV (the electric field strength of 5.67×10^5 V/m). The right-hand side electrode is at +8.5 kV (the anode) and the left-hand one is grounded (the cathode). The acquisition frame rate is 1000 fps. The dimensionless groups are We = 150.0, Oh = 0.2, K = 285.5, and $Bo_E = 2.9$.

splashing. The splash formation was nearly completely suppressed in the direction of the applied electric field. On the other hand, in the perpendicular direction, the splash formation was minimally affected. For hydrocarbon liquids, in particular, n-butanol or motor oil, the coating size could be increased in several seconds of the voltage application.

Also, the electric field diminishes propensity to the prompt splash. It affects formation of fingers at the receding stage and can suppress fingering in some cases. These phenomena are attributed to rapid ($\sim$1 μs compared to splashing $\sim$1 ms) ion redistribution to the free surface of detached liquid lamella and the emergence of an electric Coulomb force which attracts the lamella back to the substrate polarized by the electric field applied. Such a re-adjustment of the lamella to the substrate can be accompanied by tiny bubble entrapment.

Accordingly, polarization of such substrates as parafilm, pre-stretched Teflon, polypropylene, and potentially many other dielectric substrates, by an applied electric field, which facilitates the electrowetting phenomena, can be utilized in spraying of aqueous or hydrocarbon-based paints to increase surface coverage with less paint being used. In the present work, the focus is on pure liquids which revealed significant electrowetting phenomena triggered by the application of the electric field resulting in an enhanced spreading on polarized surfaces. Paints are suspensions of paint pigments in water or non-aqueous liquids. The effect of pigment particles on electrowetting of paints on polarized substrates deserves a detailed investigation in future work.

SUPPLEMENTARY MATERIAL

See the supplementary material for the experimental information on the surfaces utilized, preliminary experimental results, and modeling information.

ACKNOWLEDGMENTS

This work was supported by NSF Grant Number 1906497.

DATA AVAILABILITY

The data that support the findings of this study are available from the corresponding author upon reasonable request.

REFERENCES

[1]A. L. Yarin, "Drop impact dynamics: Splashing, spreading, receding, bouncing…," Annu. Rev. Fluid Mech. **38**, 159–192 (2006).
[2]A. L. Yarin, I. V. Roisman, and C. Tropea, *Collision Phenomena in Liquids and Solids* (Cambridge University Press, Cambridge, 2017).
[3]C. Josserand and S. T. Thoroddsen, "Drop impact on a solid surface," Annu. Rev. Fluid Mech. **48**, 365–391 (2016).
[4]R. Rioboo, M. Marengo, and C. Tropea, "Time evolution of liquid drop impact onto solid, dry surfaces," Exp. Fluids **33**, 112–124 (2002).
[5]J. Plog, J. M. Löwe, Y. Jiang, Y. Pan, and A. L. Yarin, "Control of direct written ink droplets using electrowetting," Langmuir **35**, 11023–11036 (2019).
[6]J. Park and D. E. Kim, "Dynamic Leidenfrost behaviors of different fluid drops on superheated surface: Scaling for vapor film thickness," Phys. Fluids **31**, 101702 (2019).
[7]R. Rioboo, C. Tropea, and M. Marengo, "Outcomes from a drop impact on solid surfaces," Atomization Sprays **11**, 115–165 (2001).
[8]M. Cao, D. Guo, C. Yu, K. Li, M. Liu, and L. Jiang, "Water-repellent properties of superhydrophobic and lubricant-infused 'slippery' surfaces: A brief study on the functions and applications," ACS Appl. Mater. Interfaces **8**, 3615–3623 (2016).
[9]S. Shi, C. Lv, and Q. Zheng, "Drop impact on two-tier monostable superrepellent surfaces," ACS Appl. Mater. Interfaces **11**, 43698–43707 (2019).
[10]K. Regulagadda, S. Bakshi, and S. K. Das, "Morphology of drop impact on a superhydrophobic surface with macro-structures," Phys. Fluids **29**, 082104 (2017).
[11]H. Zhang, X. Yi, Y. Du, R. Zhang, X. Zhang, F. He, F. Niu, and P. Hao, "Dynamic behavior of water drops impacting on cylindrical superhydrophobic surfaces," Phys. Fluids **31**, 032104 (2019).
[12]D. Bartolo, A. Boudaoud, G. Narcy, and D. Bonn, "Dynamics of non-Newtonian droplets," Phys. Rev. Lett. **99**, 174502 (2007).
[13]V. Bergeron, D. Bonn, J. Y. Martin, and L. Vovelle, "Controlling droplet deposition with polymer additives," Nat. **405**, 772–775 (2000).
[14]M. Aytouna, D. Bartolo, G. Wegdam, D. Bonn, and S. Rafaï, "Impact dynamics of surfactant laden drops: Dynamic surface tension effects," Exp. Fluids **48**, 49–57 (2010).
[15]K. P. Gatne, M. A. Jog, and R. M. Manglik, "Surfactant-induced modification of low Weber number droplet impact dynamics," Langmuir **25**, 8122–8130 (2009).
[16]S. Mangili, C. Antonini, M. Marengo, and A. Amirfazli, "Understanding the drop impact phenomenon on soft PDMS substrates," Soft Matter **8**, 10045–10054 (2012).
[17]S. Yun and G. Lim, "Ellipsoidal drop impact on a solid surface for rebound suppression," J. Fluid Mech. **752**, 266–281 (2014).
[18]G. Karniadakis, A. Beskok, and N. Aluru, *Microflows and Nanoflows: Fundamentals and Simulation* (Springer, Berlin, 2005).
[19]G. Beni, S. Hackwood, and J. L. Jackel, "Continuous electrowetting effect," Appl. Phys. Lett. **40**, 912–914 (1982).

[20]F. Mugele and J. C. Baret, "Electrowetting: From basics to applications," J. Phys.: Condens. Matter **17**, R705–R774 (2005).
[21]M. W. Lee, S. S. Latthe, A. L. Yarin, and S. S. Yoon, "Dynamic electrowetting-on-dielectric (DEWOD) on unstretched and stretched Teflon," Langmuir **29**, 7758–7767 (2013).
[22]V. Yurkiv, A. L. Yarin, and F. Mashayek, "Modeling of droplet impact onto polarized and nonpolarized dielectric surfaces," Langmuir **34**, 10169–10180 (2018).
[23]S. Pal, A. M. Miqdad, S. Datta, A. K. Das, and P. K. Das, "Control of drop impact and proposal of pseudo-superhydrophobicity using electrostatics," Ind. Eng. Chem. Res. **56**, 11312–11319 (2017).
[24]R. L. Vander Wal, G. M. Berger, and S. D. Mozes, "The splash/non-splash boundary upon a dry surface and thin fluid film," Exp. Fluids **40**, 53–59 (2006).
[25]D. A. Burzynski, I. V. Roisman, and S. E. Bansmer, "On the splashing of high-speed drops impacting a dry surface," J. Fluid Mech. **892**, A2, 1–30 (2020).
[26]I. Burstyn and H. Kromhout, "Trends in inhalation exposure to hydrocarbons among commercial painters in The Netherlands," Scand. J. Work, Environ. Health **28**, 429–438 (2002).
[27]J. Halstead, U.S. patent 10,370,541 (2019).
[28]H. Yang, K. Sun, Y. Xue, C. Xu, D. Fan, Y. Cao, and W. Xue, "Controllable drop splashing on picosecond laser patterned hybrid superhydrophobic/-philic surfaces," Appl. Surf. Sci. **481**, 184–191 (2019).
[29]Y. Wang and L. Bourouiba, "Drop impact on small surfaces: Thickness and velocity profiles of the expanding sheet in the air," J. Fluid Mech. **814**, 510–534 (2017).
[30]Y. Wang, R. Dandekar, N. Bustos, S. Poulain, and L. Bourouiba, "Universal rim thickness in unsteady sheet fragmentation," Phys. Rev. Lett. **120**, 204503 (2018).
[31]L. Xu, W. W. Zhang, and S. R. Nagel, "Drop splashing on a dry smooth surface," Phys. Rev. Lett. **94**, 184505 (2005).
[32]R. E. Pepper, L. Courbin, and H. A. Stone, "Splashing on elastic membranes: The importance of early-time dynamics," Phys. Fluids **20**, 082103 (2008).
[33]E. J. Vega and A. A. Castrejón-Pita, "Suppressing prompt splash with polymer additives," Exp. Fluids **58**, 57 (2017).
[34]M. Song, J. Ju, S. Luo, Y. Han, Z. Dong, Y. Wang, and L. Jiang, "Controlling liquid splash on superhydrophobic surfaces by a vesicle surfactant," Sci. Adv. **3**, e1602188 (2017).
[35]F. O. Alpak, B. Riviere, and F. Frank, "A phase-field method for the direct simulation of two-phase flows in pore-scale media using a non-equilibrium wetting boundary condition," Comput. Geosci. **20**, 881–908 (2016).
[36]D. Jacqmin, "Calculation of two-phase Navier–Stokes flows using phase-field modeling," J. Comput. Phys. **155**, 96–127 (1999).
[37]H. Ding, P. D. Spelt, and C. Shu, "Diffuse interface model for incompressible two-phase flows with large density ratios," J. Comput. Phys. **226**, 2078–2095 (2007).
[38]Y. Couder, S. Protiere, E. Fort, and A. Boudaoud, "Walking and orbiting droplets," Nature **437**, 208–208 (2005).
[39]J. Moláček and J. W. Bush, "Drops bouncing on a vibrating bath," J. Fluid Mech. **727**, 582–611 (2013).
[40]J. M. Löwe, V. Hinrichsen, I. V. Roisman, and C. Tropea, "Behavior of charged and uncharged drops in high alternating tangential electric fields," Phys. Rev. E **101**, 023102 (2020).
[41]S. T. Thoroddsen, K. Takehara, and T. G. Etoh, "Micro-splashing by drop impacts," J. Fluid Mech. **706**, 560–570 (2012).
[42]J. Wang, H. Yu, J. Shen, B. Yang, and C. Tropea, "Simulation of the optical caustics associated with the primary rainbow for oblate spheroidal drops illuminated by a Gaussian beam," Opt. Exp. **29**, 377–384 (2021).
[43]Y. Cao, W. Wang, H. Yu, J. Shen, and C. Tropea, "Characterization of refractive index and size of a spherical drop by using Gaussian beam scattering in the secondary rainbow region," J. Quant. Spectrosc. Radiat. Transfer **242**, 106785 (2020).
[44]Y. L. Hung, M. J. Wang, J. W. Huang, and S. Y. Lin, "A study on the impact velocity and drop size for the occurrence of entrapped air bubbles–water on parafilm," Exp. Therm. Fluid Sci. **48**, 102–109 (2013).
[45]G. Riboux and J. M. Gordillo, "Experiments of drops impacting a smooth solid surface: A model of the critical impact speed for drop splashing," Phys. Rev. Lett. **113**, 024507 (2014).
[46]D. Y. Chu, Q. Zhang, and R. L. Liu, "Standard Gibbs free energies of transfer of NaCl and KCl from water to mixtures of the four isomers of butyl alcohol with water. The use of ion-selective electrodes to study the thermodynamics of solutions," J. Chem. Soc., Faraday Trans. 1 **83**, 635–644 (1987).
[47]M. S. Agathou, J. W. Powell, F. L. Chia-fon, and D. C. Kyritsis, Preliminary experimental study of butanol electrosprays for power generation. SAE Paper No. 2007-24-0020, 2007.
[48]M. Pecovska-Gjorgjevich, A. Andonovski, and J. Velevska, "Measuring frequency-and temperature-dependent permittivities of vegetable oils," Phys. Maced. **59**, 77–89 (2010).
[49]A. Sankaran, C. Staszel, F. Mashayek, and A. L. Yarin, "Faradaic reactions' mechanisms and parameters in charging of oils," Electrochim. Acta **268**, 173–186 (2018).
[50]Y. Wakuri, M. Soejima, Y. Ejima, T. Hamatake, and T. Kitahara, "Studies on friction characteristics of reciprocating engines," SAE Trans. **104**, 1463–1477 (1995).